Review

Computational microscopy with coherent diffractive imaging and ptychography

https://doi.org/10.1038/s41586-024-08278-z

Received: 7 August 2023

Accepted: 23 October 2024

Published online: 8 January 2025

Check for updates

Jianwei Miao[1,2]✉

Microscopy and crystallography are two essential experimental methodologies for advancing modern science. They complement one another, with microscopy typically relying on lenses to image the local structures of samples, and crystallography using diffraction to determine the global atomic structure of crystals. Over the past two decades, computational microscopy, encompassing coherent diffractive imaging (CDI) and ptychography, has advanced rapidly, unifying microscopy and crystallography to overcome their limitations. Here, I review the innovative developments in CDI and ptychography, which achieve exceptional imaging capabilities across nine orders of magnitude in length scales, from resolving atomic structures in materials at sub-ångstrom resolution to quantitative phase imaging of centimetre-sized tissues, using the same principle and similar computational algorithms. These methods have been applied to determine the 3D atomic structures of crystal defects and amorphous materials, visualize oxygen vacancies in high-temperature superconductors and capture ultrafast dynamics. They have also been used for nanoscale imaging of magnetic, quantum and energy materials, nanomaterials, integrated circuits and biological specimens. By harnessing fourth-generation synchrotron radiation, X-ray-free electron lasers, high-harmonic generation, electron microscopes, optical microscopes, cutting-edge detectors and deep learning, CDI and ptychography are poised to make even greater contributions to multidisciplinary sciences in the years to come.

The invention of the telescope and microscope, both of which are based on lenses, had a pivotal role in driving the scientific revolution of the seventeenth century[1]. Since then, various forms of lens-based microscopy, including optical, phase-contrast, confocal, fluorescence, super-resolution, X-ray and electron microscopy, have been crucial in expanding our understanding of the microscopic world[2]. Another fundamental field is crystallography, which has greatly advanced physics, chemistry, geology, materials science, nanoscience, biology and life sciences over the past century[3]. In 1999, the methodology of crystallography was extended to determine the structure of non-crystalline samples, merging microscopy with crystallography by replacing the lens with coherent diffraction and computational algorithms[4]. This experiment, benefiting from earlier advances in crystallography[5,6], electron microscopy[7], optical phase retrieval[8–10], synchrotron radiation[11] and detector technology[12], sparked a wave of developments in CDI and modern ptychography methods[13–19]. It also initiated an ongoing international conference series on coherent scattering and phase retrieval[20]. These methods have been extensively implemented using synchrotron radiation[13–15,17], X-ray-free electron lasers (XFELs)[14,15], high-harmonic generation (HHG)[15], electron microscopy[18] and optical microscopy[19]. They have found truly multidisciplinary applications, from achieving the highest resolution in microscopy[21–24] and detecting atomic-scale defects in superconductors[25], to 3D mapping of spin textures[26–28], nanoscale strain in electrodes[29–32] and phase imaging of tissues[33,34], biominerals[35–37], cells[38–46], viruses[47–51] and proteins[52,53]. While several review articles have focused on specific subfields[13–19,54–56], to the best of my knowledge, a comprehensive review covering the entire field has not yet been published.

In this review, I present a thorough overview of the innovations in CDI and ptychography. I discuss various CDI and ptychography methods that rely on iterative phase-retrieval algorithms (Box 1 Fig. 1), which alternate between real and reciprocal space to find global solutions that are consistent with experimental measurements and constraints[16,18,55,56]. Unlike conventional microscopy, which requires wavelength-specific lenses for photons and electrons[2], CDI and ptychography utilize focusing optics to shape the incident wave into a probe function and capture diffraction patterns directly. By employing the same principle and similar phase-retrieval algorithms across the entire spectrum (Box 1), both the magnitude and the phase of the transmission functions of an object are reconstructed from these diffraction patterns. The resulting images are free of aberrations, with resolution limited only by the wavelength of the incident radiation and the spatial frequency of the diffracted waves. To illustrate the versatility and broad applicability of CDI and ptychography, I highlight several recent breakthroughs across different disciplines. These include using electron ptychography to achieve resolutions that exceed the limits of aberration-corrected electron microscopy[21–24]; quantitative characterization of point defects in high-temperature superconductors[25]; nanoscale imaging of

[1]Department of Physics and Astronomy, University of California, Los Angeles, Los Angeles, CA, USA. [2]California NanoSystems Institute, University of California, Los Angeles, Los Angeles, CA, USA. ✉e-mail: j.miao@ucla.edu

Box 1

Principle and iterative algorithms for phase retrieval

When a beam of photons or electrons hits a detector, the intensity of the beam can be measured but the phase information is lost, which is often referred to as a 'phase problem'. Holography addresses this problem by using the interference between a reference wave and an object wave to record both the amplitude and the phase of the wavefront[186]. The phase problem has also been crucial in crystallography, in which discrete peaks are diffracted from crystals. Over the years, several phasing methods have been developed, including direct methods, isomorphous replacement, molecular replacement and multi-wavelength anomalous dispersion[187]. However, unlike crystallography, CDI and ptychography involve a coherent wave that is incident on a non-crystalline sample or a confined wave illuminating a crystal, producing continuous diffraction intensity instead of discrete peaks. Solving the phase problem in these cases requires different methods. In 1952, it was suggested that sampling the continuous diffraction intensity at a frequency finer than the Nyquist interval might provide phase information[188]. In the 1970s, three Fourier-based iterative algorithms were developed for phase retrieval[7,8,189], stimulating early theoretical and computational studies on the uniqueness of the solution[9,10,190,191]. An important parameter is the overdetermination ratio, defined as $\alpha_o = M/N$, where M and N are the number of independently measured points and unknown variables, respectively. This ratio generalizes the oversampling ratio first introduced in 1998 (ref. 10). Recently, theoretical studies on the uniqueness of the solution have been revived[55,56,192,193], demonstrating that a unique solution becomes possible when $\alpha_o \geq 1$ in the absence of noise. However, because of the incompleteness of the measured data and the presence of noise, α_o must be several times larger than 1 to guarantee successful phase retrieval[55,56,193]. This requirement can be achieved through a combination of oversampling, overlapping and other constraints.

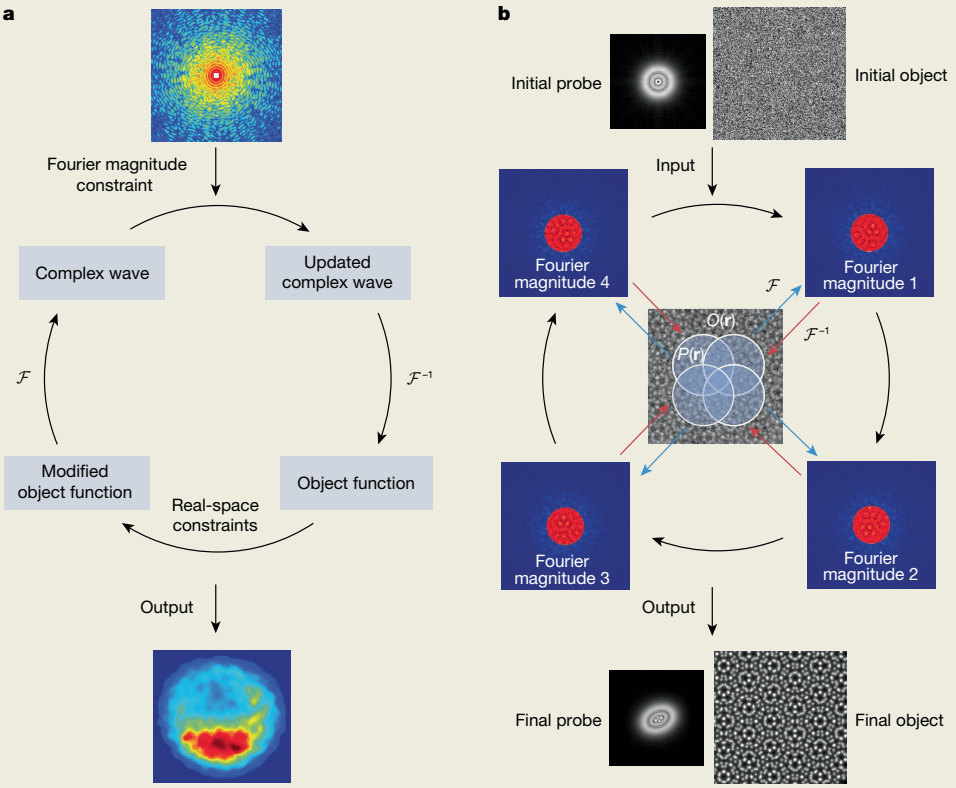

Box 1 Fig. 1 | Iterative phase retrieval for CDI and modern ptychography. a,**b**, Schematic diagrams of iterative phase-retrieval algorithms for CDI (**a**) and modern ptychography (**b**), where $\mathcal{F}$ is the Fourier transform, $\mathcal{F}^{-1}$ is the inverse Fourier transform, $P(\mathbf{r})$ is a probe function and $O(\mathbf{r})$ is an object function.

Currently, phase retrieval in CDI and ptychography predominantly relies on Fourier-based iterative algorithms, including the Gerchberg–Saxton algorithm[7], error reduction[8,189], hybrid input–output[8,189], a difference map[194], a shrinkwrap[76], relaxed averaged alternating reflectors[195], oversampling smoothness[196], an extended ptychographic iterative engine[197], maximum likelihood[198,199] and others[16,18]. The schematic of the iterative algorithms for CDI, in which the measured Fourier magnitude is combined with a random phase set to create a complex wave, is shown in Box 1 Fig. 1a. Applying the inverse Fourier transform, $\mathcal{F}^{-1}$, to the complex wave generates an object function, which is modified by imposing real-space constraints, such as support, positivity and sparsity[8,16,200]. By taking the Fourier transform, $\mathcal{F}$, of the modified object function, a new complex wave is obtained. The magnitude of the complex wave is replaced by the measured Fourier magnitude but retains the phase, producing an updated complex wave for the next iteration. After several hundred or thousands of iterations, the algorithms generally converge to final solutions.

Box 1 Fig. 1b shows the basic principle of the iterative algorithms for modern ptychography[18,197], which starts with initial guesses of a probe, $P(\mathbf{r})$, and an object function, $O(\mathbf{r})$. Multiplication of these two functions at a scan position results in an exit wave. Applying the Fourier transform to the exit wave produces a complex wave, which is modified by replacing its magnitude with the measured Fourier magnitude. The inverse Fourier transform of this modified complex wave generates a new exit wave, which updates the probe and object functions. These updated functions are then used as inputs for the next scan position, as shown in Box 1 Fig. 1b with four scanning positions. A single macro iteration is completed after processing all the scan positions. Modern ptychography combines oversampling in reciprocal space with overlapping in real space to achieve $\alpha_o \gg 1$, allowing the algorithms to converge rapidly after tens or hundreds of macro iterations. These algorithms can also be applied to Fourier ptychography, which extends iterative phase retrieval to full-field imaging set-ups by exchanging constraints in real and reciprocal space[19]. Fourier-based iterative algorithms, also known as alternating projection algorithms, are widely used in CDI and modern ptychography, but convex optimization methods, such as PhaseLift[201], PhaseCut[202] and others[55], have also been developed for phase retrieval. Despite their computational complexity limiting practical application, these methods have spurred intense study in numerical algorithms for phase retrieval in applied mathematics[55,56,192,193].

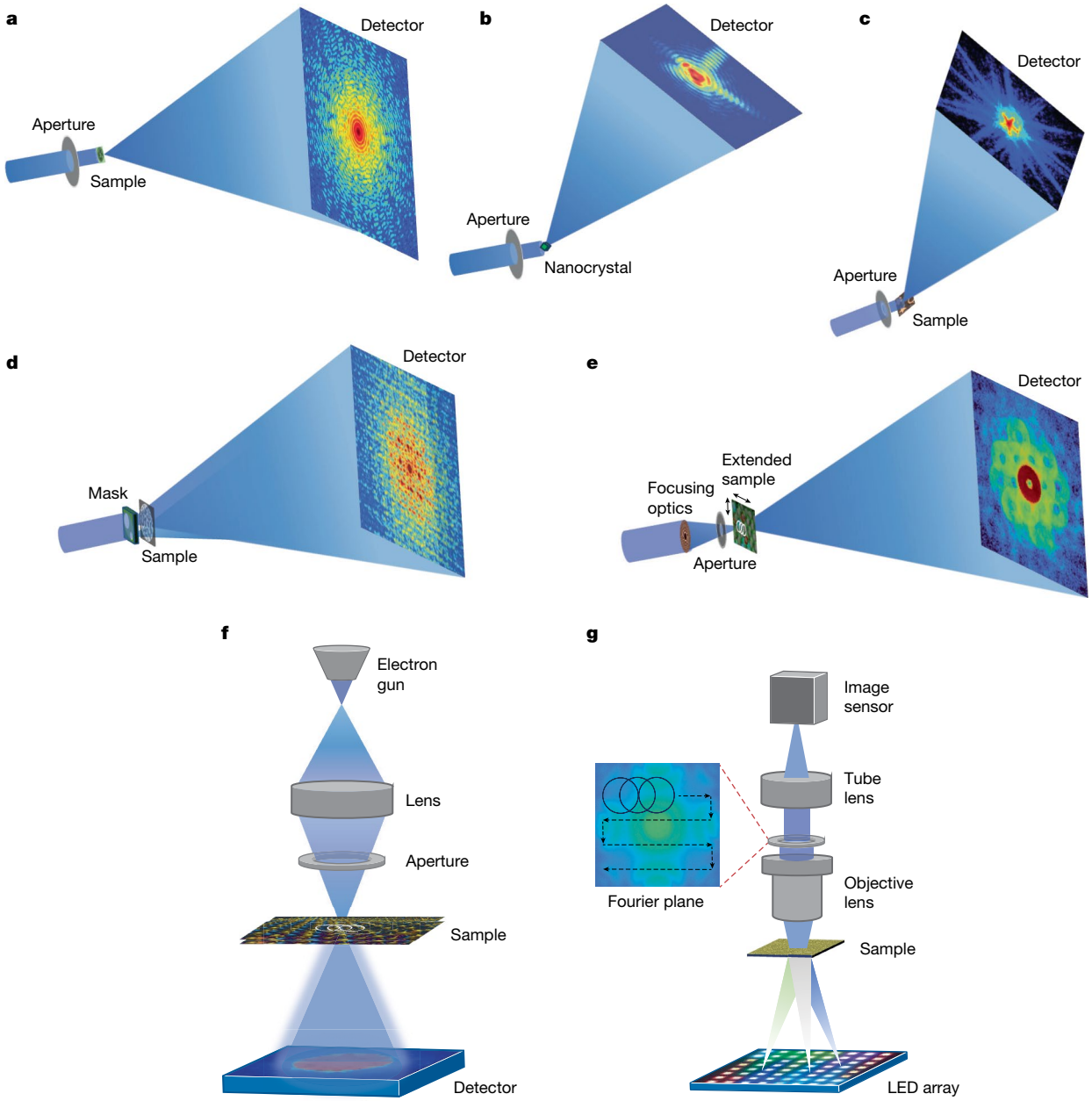

Fig. 1 | Schematics of representative CDI and modern ptychography methods. a, Conventional CDI. A coherent wave illuminates a sample and the detector records an oversampled diffraction pattern. **b**, Bragg CDI. Diffraction patterns around one or multiple Bragg peaks are collected from a nanocrystal. **c**, Reflection CDI. The diffraction pattern is measured from a surface or interface using reflection or grazing incidence geometry. **d**, Holographic CDI. The diffraction pattern arising from both an object and a reference wave is acquired, and iterative phase-retrieval algorithms are used to overcome the limitations of holography. **e**, X-ray ptychography. An X-ray probe raster-scans an extended sample, with each probe overlapping the adjacent ones, and a detector records the diffraction pattern at each scan position. **f**, Electron ptychography. A focused electron beam scans the sample, collecting a series of diffraction patterns from partly overlapping regions. **g**, Fourier ptychography. An LED array illuminates the sample from various angles, generating a series of confined Fourier spectra, which are selected by an aperture to produce a sequence of images on an image sensor.

magnetic, quantum and battery materials[26–32,57–61], nanomaterials[36,62,63] and integrated circuits[64–66]; quantitative phase imaging of biological specimens[33–53,67,68]; and capturing ultrafast phenomena[59,61,69,70]. Finally, I provide insights into the future directions of this rapidly expanding multidisciplinary field, which is expected to have an even more profound impact on science and technology in the coming years.

CDI and modern ptychography

CDI methods

When a coherent wave illuminates a non-crystalline sample or a nanocrystal, the far-field diffraction pattern is continuous and can be sampled at a frequency finer than the Nyquist interval (that is, the inverse of the sample size). When the number of independently measured points exceeds the number of unknown variables by a sufficient amount[10], the phases can, in principle, be retrieved from the diffraction pattern (Box 1). This method, known as CDI or lensless imaging[4], has been implemented in various configurations, including conventional CDI (cCDI)[15], Bragg CDI (BCDI)[13], reflection CDI (RCDI)[15], Fresnel CDI[71], coherent modulation imaging[72] and holographic CDI (HCDI)[73,74]. In cCDI, the forward diffraction pattern of a sample is recorded by a detector (Fig. 1a), followed by phasing to reconstruct its image (Box 1 Fig. 1a). By tilting the sample at different orientations, a series of diffraction patterns can be collected to reconstruct the 3D structure

of the sample[75]. cCDI has been successfully implemented using synchrotron radiation[42,43,45,47,75–77], XFELs[48–50,52,78], HHG[79–81] and electron microscopy[82–85]. A major advantage of cCDI is its ability to perform single-shot diffractive imaging by capturing the diffraction pattern from an XFEL pulse before the sample is destroyed[78,86]. Furthermore, the use of plane-wave illumination ensures that the diffraction pattern remains translation invariant with the sample, greatly simplifying the sample alignment process during image reconstruction. However, a limitation of cCDI is the necessity for isolated objects or the use of a finite beam to define the sample size.

BCDI harnesses the coherent diffraction pattern of a nanocrystal, which oscillates around each Bragg peak, owing to the finite size of the sample[87,88]. By rocking the nanocrystal relative to an X-ray beam, the 3D diffraction patterns around one or multiple Bragg peaks can be measured and then phased to obtain the 3D complex density of the nanocrystal (Fig. 1b). The amplitude and phase of the complex density correspond to the shape and lattice deformation of the nanocrystal, respectively, making it possible to determine the nanocrystal's strain[13]. A unique feature of BCDI is its ability to probe the 3D strain, lattice dynamics and dislocation propagation inside nanocrystals in response to external stimuli[29,31,36]. RCDI extends the applicability of BCDI to non-crystalline samples[89–92]. By measuring coherent diffraction patterns from a surface or interface using reflection or grazing incidence geometry (Fig. 1c), the amplitude and phase of the surface exit wave can be reconstructed. RCDI is particularly suited for coherent extreme ultraviolet sources based on HHG and can be combined with ptychography to map the 3D surface morphology and interface structure of extended samples with chemical sensitivity[93–95]. Compared with other surface-sensitive techniques, such as scanning electron microscopy and atomic force microscopy, RCDI offers the distinct advantage of providing quantitative phase information about surface and interface structures. Moreover, it has the potential to use ultrafast pulses from HHG to investigate heat, charge and spin transport in materials with high spatiotemporal resolution[95].

Fresnel CDI uses focusing optics to create a curved wave to illuminate a sample, and the resulting Fresnel diffraction pattern is measured by a detector[71,96]. When the curved incident wave is predetermined, the complex density of the sample can be reconstructed by phase-retrieval algorithms with fast and robust convergence (Box 1). Another method of achieving rapid and robust convergence is coherent modulation imaging[72], which modifies cCDI by inserting a wavefront modulator between the sample and the detector. The modulator enhances phase-retrieval convergence, relaxes the detector's dynamic range requirements, and increases tolerance to missing data. By using iterative phase-retrieval algorithms to reconstruct the amplitude and phase of a hologram (Box 1), HCDI resolves the twin-image problem in in-line holography[73,74] (the mixture of an image and its complex conjugate) and surpasses the resolution limit in off-axis holography[58,61,97] (Fig. 1d). Table 1 summarizes the advantages, current limitations and applications of various CDI and ptychography methods. The rapid development of these methods has been driven by cutting-edge detector technologies, including hybrid pixel detectors and pixel array detectors[98,99]. An important development is the electron microscopy pixel-array detector (EMPAD)[99], featuring a 128 × 128 pixel array, a dynamic range of 10^6 electrons per pixel and a frame rate of 1.1 kHz. This advancement has increased the resolution and sensitivity of electron ptychography. More recently, the next-generation charge-integrating X-ray detector, named CITIUS[100], has been introduced. With its 728 × 324 pixel array, a peak signal capacity of 1,840 photons per pixel per frame and a frame rate of 17.4 kHz, CITIUS is expected to greatly improve the data acquisition speed and image quality of X-ray CDI and ptychography.

Another computational method that benefits from CDI is the development of advanced iterative algorithms for tomography. In many tomography applications, data acquisition is constrained by the radiation dose required and the geometric limitations of the tilt range. Accurately reconstructing 3D structures from incomplete and noisy data poses a challenge comparable to phase retrieval from diffraction patterns (Box 1). In 2012, using an oversampling-based iterative algorithm[101], atomic electron tomography (AET) was developed to achieve 3D resolution at 2.4 Å without assuming crystallinity or averaging[102]. This technique iteratively searches for optimal solutions that satisfy both the measured data and the constraints[101,103]. Over the years, more-powerful iterative algorithms have been developed to enhance the 3D reconstruction[104] and precisely localize the 3D coordinates of individual atoms in materials[103]. A breakthrough in AET is its ability to determine the 3D atomic structure of amorphous materials[105,106], addressing a long-standing challenge in the physical sciences. Furthermore, integrating ptychography with AET, which is referred to as pAET, offers the potential to resolve the 3D positions of light atoms in radiation-sensitive materials[107,108], paving the way for advanced characterization of a wide range of materials.

From conventional to modern ptychography

Ptychography, derived from the Greek words *ptycho*, meaning 'to fold', and *graphein*, meaning 'to write', was proposed in 1969 to solve the phase problem in electron diffraction from crystals[109]. When a small coherent beam illuminates a crystal, the far-field diffraction pattern comprises a series of Bragg diffraction spots. These spots arise from the convolution of the Bragg peaks diffracted from the crystal and the Fourier transform of the illumination function of the beam. Increasing the convergence of the incident beam enlarges the diffraction spots, enabling them to overlap. The region of overlap can be used to estimate the phase difference between each pair of diffraction spots, except for an ambiguity involving its complex conjugate. This ambiguity can be eliminated by slightly shifting the incident beam to create a second overlap region. Although extending the method to non-crystalline samples was suggested, no general solution was proposed, owing to the absence of Bragg diffraction in these samples[110]. Over the next 38 years, ptychography was sporadically implemented with non-iterative phase-retrieval methods, such as Wigner distribution deconvolution[18,111–113]. A breakthrough came in 2007 with the experimental realization of modern ptychography[114], using an iterative phase-retrieval algorithm[115].

Modern ptychography initially combined scanning transmission X-ray microscopy with CDI, also known as ptychographic CDI[15,17,114]. In this implementation, an X-ray probe scans an extended sample, with each probe overlapping adjacent ones (Fig. 1e). A detector collects a sequence of 2D diffraction patterns, from which the magnitude and the phase of the probe and the sample transmission functions are simultaneously reconstructed by iterative phase-retrieval algorithms[17,18,116] (Box 1 Fig. 1b). Despite retaining the name, modern ptychography fundamentally differs from its original conception[109,110] for four key reasons. First, modern ptychography leverages oversampled diffraction patterns in reciprocal space and overlapping regions in real space to achieve an overdetermination ratio substantially greater than 1, enabling rapid and robust phase retrieval (Box 1). Second, conventional ptychography typically requires prior knowledge of the probe function and a scanning step size that is half the resolution[111]. By contrast, modern ptychography uses iterative algorithms to simultaneously reconstruct both the probe and the object functions[116]. This development allows for a considerable increase in the scanning step size and the field of view (FOV), with resolution limited only by the highest spatial frequency of the diffraction pattern. Third, modern ptychography incorporates a mixed-state approach to address partial coherence and measurement imperfections[117], resulting in more-precise reconstruction of both the probe and the object functions. Furthermore, advanced algorithms are used to correct for probe position errors caused by mechanical drift or stage inaccuracies, greatly enhancing the fidelity of the reconstructed images[118,119]. Finally, conventional 3D structure determination requires either sample tilting, as used in

Table 1 | Advantages, current limitations and applications of various CDI and ptychography methods

Method	Advantages	Current limitations	Applications
Conventional CDI	Enables single-shot diffractive imaging; achieves high spatial and temporal resolution; provides translation invariance with the sample	Requires isolated objects or finite beams; relies on large detectors with high dynamic ranges; necessitates computationally intensive phase retrieval	Nanomaterials, quantum and energy materials; dynamics and ultrafast phenomena; biological specimens, including cells, cellular organelles, viruses and proteins
Bragg CDI	Enables 3D strain mapping with nanoscale resolution; offers high sensitivity to lattice distortions and defects; supports advanced in situ and operando studies	Requires crystalline or polycrystalline samples; demands complex experimental set-up and data acquisition; involves computationally intensive phase retrieval	Nanomaterials and battery materials; defect dynamics in materials; catalysts; thin films; biominerals
Reflection CDI	Extends BCDI to non-crystalline samples; enables 3D mapping of extended surfaces when combined with ptychography; provides quantitative phase information of surfaces	Demands specialized beamlines and instruments; involves increased complexity in data acquisition; necessitates sophisticated algorithms for X-ray grazing incidence geometry	Nanoparticles; semiconductor nanostructures; thin films; liquid surfaces; interfaces; catalysts
Holographic CDI	Enhances the image quality and resolution of holography; facilitates rapid phase retrieval; achieves high spatiotemporal resolution; enables low-dose imaging	Requires high coherence of the illuminating source; demands precise experimental conditions such as stability and alignment; encounters challenges in achieving accurate 3D imaging	Magnetization dynamics; phase transitions in quantum materials; fluctuating states in materials; biological specimens, such as tissues and cells
X-ray ptychography	Reconstructs both the probe and the complex transmission function; achieves a large FOV with nanoscale resolution; utilizes a mixed-state approach to account for partial coherence and imperfect measurements	Demands sophisticated and stable experimental set-ups; involves long data acquisition times, which limits its use in dynamic studies; requires advanced algorithms along with substantial computational resources	Magnetic, quantum and energy materials; nanomaterials and catalysts; advanced nanoelectronics such as integrated circuits; biological specimens, such as biominerals, neuronal tissues, cells and cellular ultrastructure
Electron ptychography (4D-STEM)	Achieves the highest resolution in microscopy; reconstructs both the probe and the complex transmission function; enables 3D reconstruction with multislice ptychography; offers electron dose-efficient imaging technique; employs analytical phase recovery using Wigner distribution deconvolution and single sideband	Demands advanced detectors, precise sample positioning and stability; involves extended data acquisition times; requires advanced algorithms and substantial computational resources; necessitates fine scanning step sizes for Wigner distribution deconvolution and single sideband, which are less accurate than iterative phase retrieval	Crystal defects in 2D materials, semiconductors and superconductors; energy, magnetic, ferroelectric materials and nanomaterials; radiation-sensitive and light-element materials, such as catalysts, oxides, MOFs and polymers
Cryo-electron ptychography	Provides phase contrast for light elements such as C, N and O; achieves high resolution over a large FOV; enables imaging of thicker biological specimens through multislice reconstruction; eliminates the need for contrast transfer function correction	Faces challenges with cryo-sample vibration and drift; requires extended data acquisition times; necessitates advanced phase-retrieval and 3D image reconstruction algorithms to address low signal-to-noise ratios; demands substantial computational resources	Structural biology: macromolecules and viruses; cell biology: cellular structures, organelles and protein complexes; neuroscience: neural structures, synapses and protein aggregates; radiation-sensitive materials: batteries, organic–inorganic nanostructure and soft matter
Fourier ptychography	Greatly enhances the SBP of optical microscopy; enables quantitative phase imaging of thicker biological specimens; achieves 3D imaging without the need for sample tilting or through-focus series	Necessitates complex experimental implementation; Demands high computational resource; suffers from reduced depth resolution, owing to the 'missing cone' problem in 3D imaging; exhibits low dose efficiency	Quantitative phase imaging of tissues, multicellular organisms, cells and subcellular structures; digital pathology and cytometry; aberration metrology and surface inspection; applications in X-ray and electron microscopy

tomography and crystallography, or a through-focus series, as used in confocal microscopy. In 2010, ankylography was introduced as a means of extracting 3D structural information from a single view[120]. Despite initial controversy[121,122], this novel concept has been adopted into multislice ptychography[22,123–125], which enables the extraction of 3D structural information from thick samples without the need for sample tilting or a through-focus series.

Building on these unique capabilities, modern ptychography has been integrated into various imaging techniques (Table 1). By harnessing the penetrating power of X-rays, ptychography combined with tomography enables quantitative 3D imaging of nanomaterials[62], biological specimens[34,35,46] and integrated circuits[64,66] at the nanoscale. Furthermore, vector ptychographic tomography, combined with X-ray magnetic circular dichroism, has been developed to map 3D magnetization fields and visualize topological defects in magnetic materials[26–28]. In 2018, modern ptychography was advanced through the implementation of scanning transmission electron microscopy[2] (STEM) with a cutting-edge pixel array detector[99], a technique also referred to as 4D STEM[126] (Fig. 1f), achieving a resolution of 0.39 Å[21]. The resolution was further improved to 0.23 Å using multislice ptychography[22]. Modern ptychography has also been successfully applied to an uncorrected electron microscope, achieving a resolution surpassing that of aberration-corrected electron microscopy[24]. Furthermore, ptychography is highly dose efficient, collecting nearly all the electrons and allowing the imaging of radiation-sensitive materials at atomic resolution[127–133]. These developments highlight the power of modern electron ptychography to characterize a wide range of materials with unprecedented resolution and sensitivity.

Fourier ptychography

Lens-based microscopy has a critical trade-off between the FOV and the resolution. A large FOV requires a low numerical aperture of the objective lens, and achieving higher resolution necessitates a higher numerical aperture[19]. This trade-off is quantified by the space–bandwidth product (SBP), which is defined as the product of the resolution and the spatial extent of the acquired image. For conventional optical microscopes, the SBP is typically on the order of 10 megapixels[19]. In 2013, Fourier ptychography (FP) was developed to greatly enhance

the SBP of optical microscopy[33], although a non-iterative implementation of the method had previously been demonstrated using electron microscopy[134,135]. As the reciprocal counterpart of modern ptychography[136], FP scans the Fourier spectrum across an aperture in reciprocal space and captures images in real space[19], whereas modern ptychography scans a probe in real space and collects diffraction patterns in reciprocal space[18]. Specifically, FP uses a coherent wave to illuminate a sample at an incident angle, producing a 2D Fourier spectrum at the focal plane of the objective lens (Fig. 1g). An aperture positioned at the focal plane selects a confined Fourier spectrum to generate an image. Changing the incident angle of the illumination shifts the Fourier spectrum relative to the aperture. By varying the incident angle, a series of confined Fourier spectra, each overlapping with adjacent ones, are selected by the aperture to yield a sequence of images on a sensor. When the overdetermination ratio is larger than 1 by a sufficient amount, achieved through a combination of overlapping in reciprocal space and oversampling in real space, the magnitude and phase of the entire Fourier spectrum can be reconstructed from the acquired images using iterative phase-retrieval algorithms (Box 1).

FP was initially implemented by replacing the illumination unit of a conventional optical microscope with a light-emitting diode (LED) array. By sequentially turning on one LED at a time, a series of low-resolution images were captured to reconstruct the complex-valued object[33] (Fig. 1g). However, this implementation required long acquisition times, often on the order of minutes. This drawback was overcome by reducing data redundancy and using multiplexed illumination[137], in which multiple LEDs are randomly illuminated simultaneously to capture each image. Other high-speed data acquisition schemes have also been implemented, including laser-based illumination, parallel acquisition with multiple cameras and single-shot recording[19]. These developments have reduced the acquisition time for FP, enabling the imaging of live samples in vitro[39]. The captured low-resolution images are then processed using iterative phase-retrieval algorithms to reconstruct complex-valued objects (Box 1), enabling the rapid creation of gigapixel-sized images without the need to scan the sample. The resolution (d) of FP is defined[19,40] as $d = \lambda/(NA_{obj} + NA_{ill})$, where λ is the illumination wavelength, and NA_{obj} and NA_{ill} are the numerical apertures of the objective lens and the maximum illumination angle, respectively. This formula represents a substantial improvement in resolution over conventional optical microscopy.

The conceptual innovations developed in modern ptychography can also be incorporated into the data-processing and phase-retrieval algorithms used in FP. These include simultaneous reconstruction of the probe and object functions[116], correction for position errors[118,119] and the use of a mixed-state approach to address partial coherence and imperfect measurements[117]. These innovations have improved the accuracy of the method by computationally correcting pupil and optical aberrations, intensity variation and the incident angle of the LEDs. Furthermore, by integrating ankylography[120], multislice reconstruction[123] and diffraction tomography[138], FP can extract 3D structural information without the need for sample tilting or through-focus series[41,139,140]. These advances have established FP as a non-invasive, label-free method for the quantitative phase imaging of tissues, multicellular organisms, cells and subcellular structures, achieving gigapixel-scale SBPs (Table 1).

Multidisciplinary applications

Achieving the highest resolution in microscopy

In 2018, modern ptychography combined with STEM surpassed the resolution of aberration-corrected electron microscopy[21]. This was achieved by raster-scanning an 80 keV electron probe across twisted bilayer MoS_2 and recording diffraction patterns at each position using an EMPAD detector[99], capturing signals up to 107 mrad. Through iterative phase retrieval (Box 1 Fig. 1b), both the probe function and the phase image of the sample were reconstructed from the diffraction patterns. The reconstructed phase image of twisted bilayer MoS_2 is shown in Fig. 2a, revealing varying interatomic distances between the molybdenum atoms. The resolution of 0.39 Å is 2.5 times higher than that of aberration-corrected electron microscopy under the same imaging conditions. The resolution was further enhanced by using multislice ptychography[22], in which a defocused electron probe at 300 keV was scanned across a $PrScO_3$ crystal 21 nm thick. Diffraction patterns were recorded by the EMPAD detector[99], and multislice ptychographic phase retrieval was applied for reconstruction. The phase image of the $PrScO_3$ crystal is shown in Fig. 2b with a resolution of 0.23 Å after summing all the slices. Line scans along the Pr–Pr dumbbell and O–Sc–O directions indicate that all the atomic species, including oxygen atoms, are well resolved (Fig. 2c). Further innovations in electron ptychography have since pushed the information limit to 0.14 Å by representing atoms with Gaussian functions, modelling the electron probe using aberration coefficients and correcting misalignment between the probe direction and the zone axis of the crystal[23,141].

Electron ptychography not only achieves the highest resolution, but also provides better dose efficiency than other electron microscopy methods. It has been applied to the quantitative atomic-scale imaging of light elements in materials such as zeolites[129,132,133], superconductors[25], metal–organic frameworks[131] and electrodes[127]. The multislice ptychographic reconstruction of a zeolite 40 nm thick at 0.85 Å resolution, using a dose of 3,500 $e^- Å^{-2}$, is shown in Fig. 2d. The reconstruction reveals the positions of oxygen atoms and the orientations of adsorbed molecules[133]. Energy-filtered multislice ptychography has also been advanced to detect oxygen vacancies in $La_3Ni_2O_{7-\delta}$, a material that exhibits high-transition-temperature superconductivity at around 80 K under high pressure[25]. A ptychographic phase image of a 6 Å slice of $La_3Ni_2O_{7-\delta}$ at a depth of 6.6 nm is shown in Fig. 2e,f, revealing oxygen vacancies at the inner apical sites of the NiO_6 octahedra. Furthermore, by combining multislice ptychography with electron energy-loss spectroscopy, a correlation is established between nanoscale stoichiometry and electronic structure. These results are expected to stimulate further theoretical and experimental studies to reveal the pairing mechanism of superconducting nickelate materials under high pressure. Although multislice ptychography shows great promise, its current primary limitation is a much lower depth resolution than lateral resolution[22,120,125]. However, combining ptychography with AET can overcome this limitation[107,108], which would enable 3D atomic-structure determination of light elements and radiation-sensitive materials.

The 3D atomic structure of crystal defects and amorphous materials

By incorporating iterative algorithms from CDI into tomographic reconstruction[101], AET has become the highest-resolution method for resolving the 3D structure of crystal defects and disordered materials[102,103]. In 2021, AET was advanced to determine the 3D atomic structure of amorphous materials[105]. The 3D atomic arrangement of a multi-component metallic glass composed of eight elements is shown in Fig. 2g. The elements were categorized into three types on the basis of their atomic numbers: cobalt and nickel as type 1; rubidium, rhodium, palladium and silver as type 2; and iridium and platinum as type 3. Type-3 atoms act as solute centres, surrounded by type-1 and type-2 solvent atoms, forming short-range order clusters. Some of these clusters connect to create medium-range order (Fig. 2h). Four types of medium-range order were identified in the metallic glass: face-centred cubic, hexagonal close-packed, body-centred cubic and simple cubic. AET was also used to resolve the 3D atomic structure of monatomic amorphous materials, including a tantalum thin film and two palladium nanoparticles[106]. A quantitative analysis revealed pentagonal bipyramids as the predominant atomic motifs in these materials. Contrary to conventional understanding, these pentagonal bipyramids do not assemble into complete icosahedra but

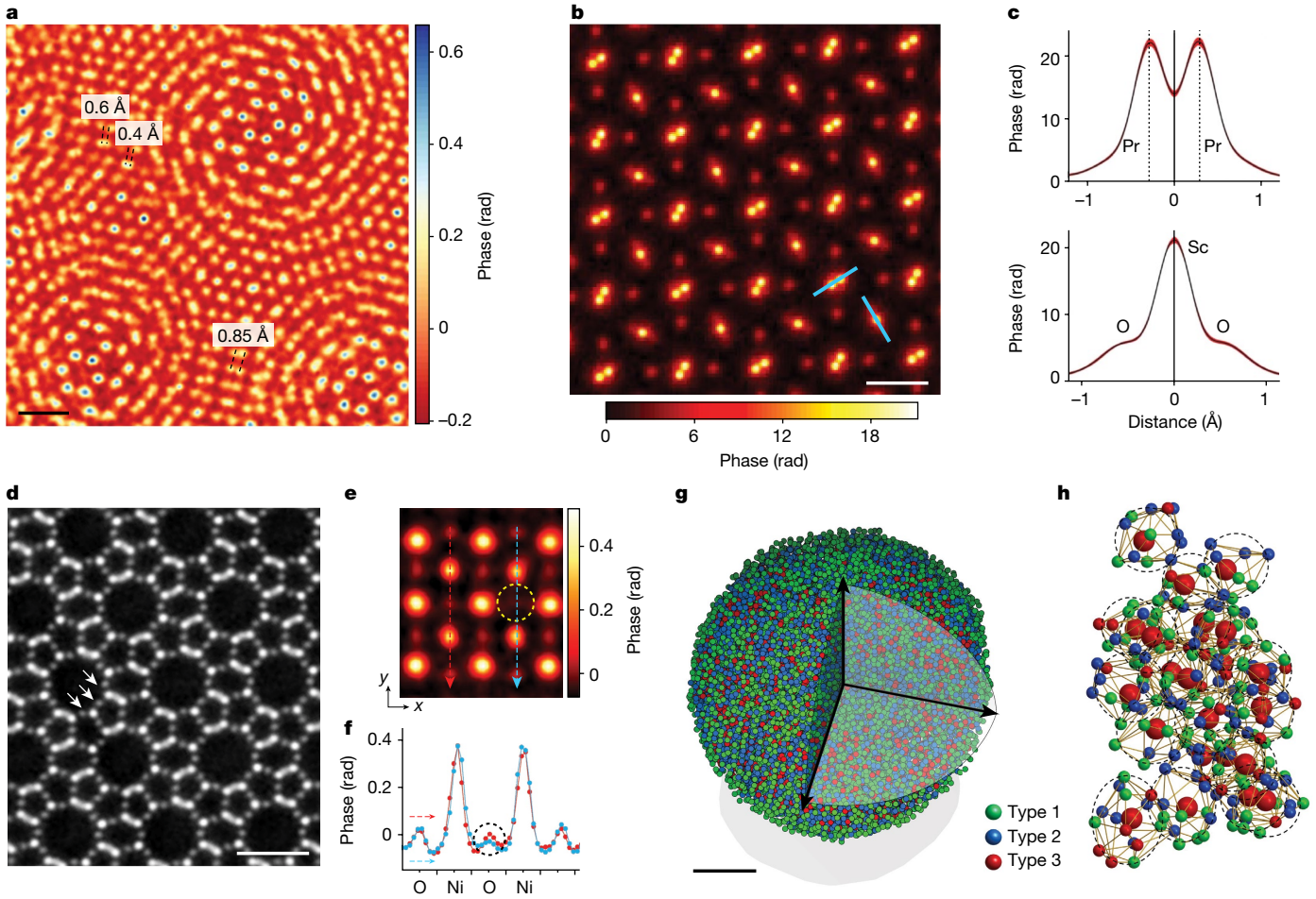

Fig. 2 | The 2D and 3D atomic-scale imaging of materials. a, Ptychographic reconstruction of twisted bilayer MoS_2 at 0.39 Å resolution[21]. Scale bar, 5 Å. **b**, Multislice ptychographic reconstruction of a $PrScO_3$ sample 21 nm thick along the [001] direction[22]. The two blue lines relate to the graphs in **c**. Scale bar, 2 Å. **c**, Line scans along the Pr–Pr dumbbell and O–Sc–O directions, corresponding to the two blue lines in **b**. **d**, Multislice ptychographic reconstruction of a Zeolite Socony Mobil-5 catalyst along the [010] direction[133], resolving all atoms, including the oxygen atoms indicated by the white arrows. Scale bar, 1 nm. **e**, Phase image of a 6 Å slice of $La_3Ni_2O_{7-\delta}$ at a depth of 6.6 nm from the surface, obtained by multislice ptychography[25]. Large, intermediate and small blobs represent lanthanum, nickel and oxygen atoms, respectively. The coloured arrows relate to the graph in **f** and the dashed circle indicates oxygen vacancies at the inner apical sites. **f**, Line scans along the red and blue arrows in **e**, illustrating the quantitative phase variation between nickel and oxygen atoms. The dashed circle denotes the phase change resulting from oxygen vacancies at the inner apical sites. **g**, 3D atomic structure of a metallic glass nanoparticle resolved by AET[105]. Scale bar, 2 nm. **h**, One of four types of medium-range order observed in the metallic glass nanoparticle. Short-range-order clusters (dashed circles) exhibit translational order but lack orientational order[105]. Images in **a** and **e**–**h** reproduced from refs. 21 (**a**), 25 (**e** and **f**) and 105 (**g** and **h**), Springer Nature Limited; images in **b** and **c** reproduced from ref. 22, American Association for the Advancement of Science; image in **d** adapted from ref. 133, American Association for the Advancement of Science.

instead interlink to form networks that extend into medium-range order.

More recently, AET has been used to determine the 3D atomic positions and local chemical order of medium- and high-entropy alloy nanoparticles, revealing lattice distortion, strain tensors, dislocations, twin boundaries and chemical short-range order in 3D detail[142]. The twin boundaries were induced by the chemical short-range order, marking the first experimental observation of structural defects correlating with chemical order. AET was also used to determine the surface morphology, local atomic structure and chemical composition of platinum-alloy nanocatalysts at the single-atom level[143]. The experimentally measured 3D atomic coordinates and chemical species were input directly into density functional theory (DFT)-trained machine-learning models to identify the surface active sites of the nanocatalysts. These ground-breaking experiments have shown that, with powerful computational methods and advanced electron microscopes, AET greatly increases our understanding of structure–property relationships in materials. Moreover, by integrating ptychography with AET, pAET has the potential to extend this capability to a broader range of materials, including radiation-sensitive ones, enabling deeper insights into their 3D atomic structures.

Nanoscale imaging of quantum materials and magnetization dynamics

Quantum materials exhibit exotic electronic, magnetic, optical and topological properties as the result of interactions between charge, spin, orbit and lattice degrees of freedom[144]. The coupling of electron spin and orbital motion gives rise to magnetic spin textures such as vortices, skyrmions, hedgehogs and hopfions, which are of great interest for both fundamental research and technological applications[26–28,57,145]. By integrating X-ray magnetic linear and circular dichroism, CDI and ptychography have enabled the 2D and 3D imaging of these magnetic spin textures. Figure 3a illustrates the 3D spin textures of a Bloch point, also known as a hedgehog or topological magnetic monopole (TMM), initially revealed by vector ptychographic tomography at a resolution of 100 nm (ref. 26). Improvements have since increased the 3D resolution to 10 nm (Fig. 3b), enabling quantitative characterization of the

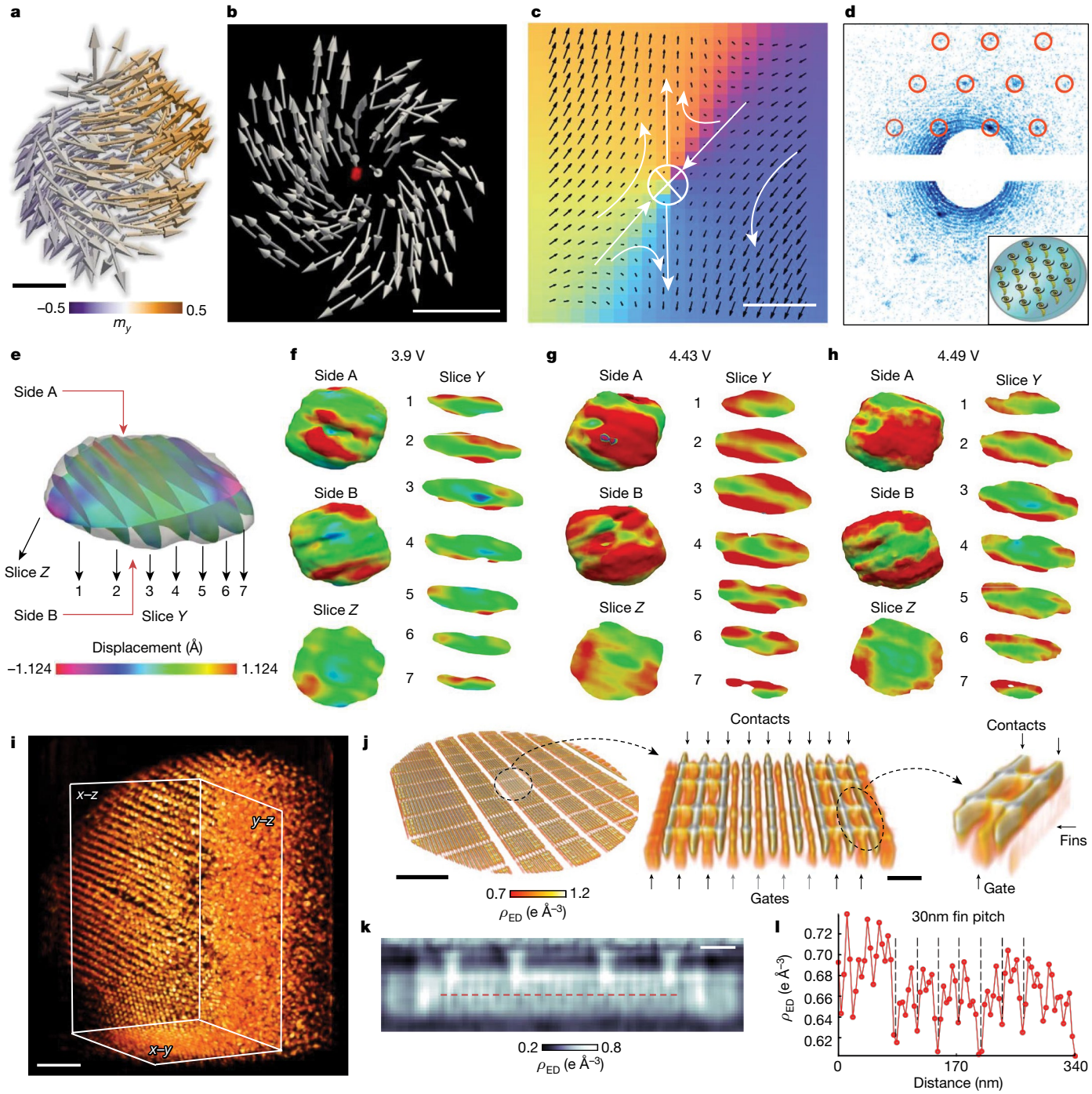

Fig. 3 | Nanoscale imaging of quantum materials, electrodes, nanomaterials and integrated circuits. a,**b**, 3D images of topological spin textures of a Bloch point (also called a hedgehog or a TMM) at a resolution of 100 nm (ref. 26) (**a**) and 10 nm (ref. 28) (**b**). m_y in **a** represents the *y*-component of the magnetization. Scale bars, 100 nm (**a**), 10 nm (**b**). **c**, Magnetic field at the boundary between two skyrmions. White arrows and a cross illustrate an anti-vortex point[57]. Scale bar, 2 nm. **d**, Single-shot CDI for imaging quantum vortices, illustrating a representative diffraction pattern of a helium-4 droplet doped with xenon atoms[60]. The distribution of the Bragg spots (highlighted by red circles) indicates that the xenon atoms are condensed around the cores of multiple quantum vortices (inset). **e**–**h**, 3D in situ observation of strain evolution in lithium-rich layered oxide cathodes[31] (**e**), measured at 3.9 V (**f**), 4.43 V (**g**) and 4.49 V (**h**). **i**, 3D imaging of a nanoparticle superlattice, revealing grain structure and a disordered region near the centre[62]. Scale bar, 200 nm. **j**, Non-destructive quantitative 3D imaging of a 7 nm integrated circuit[66], showing the lowest layer of the integrated circuit, a characteristic transistor unit cell and fin field-effect transistor components; ρ_{ED} is the electron density. Scale bars, 1 µm (left), 100 nm (right). **k**, Cross-section of the 3D reconstruction across the fins (indicated by the horizontal arrow labelling the fins in **j**). Scale bar, 50 nm. **l**, Line scan along the dashed line in **k**, displaying the variation in electron density of the 30-nm fin pitch. Images in **a**, **b**, **c** and **j**–**l**, reproduced from refs. 26 (**a**), 28 (**b**), 57 (**c**) and 66 (**j**–**l**), Springer Nature Limited; image in **d** adapted from ref. 60, American Association for the Advancement of Science; images in **e**–**h** adapted from ref. 31, Springer Nature Limited; image in **i** reproduced from ref. 62, American Association for the Advancement of Science.

3D spin textures of 138 TMMs and anti-TMMs in a ferromagnetic metal lattice[28]. The analysis revealed that TMM–anti-TMM pairs stabilize at shorter distances than do TMM–TMM or anti-TMM–anti-TMM pairs.

To achieve higher resolution, Lorentz electron ptychography has been demonstrated to image magnetic spin textures near skyrmion cores, boundaries and dislocations with nanometre-scale resolution[57] (Fig. 3c).

Furthermore, AET has been used to determine the 3D coordinates of the iron and platinum atoms in an FePt alloy nanoparticle with 22 picometre precision[146]. These 3D atomic coordinates were used in DFT calculations to correlate chemical order and disorder with magnetic properties such as atomic spin and orbital magnetic moment, and local magnetocrystalline anisotropy.

Although high-resolution imaging of spin textures deepens our understanding of topological magnetic defects, probing magnetization dynamics is equally important. HCDI enables the simultaneous imaging of magnetic structures and dynamics by recording time-series diffraction patterns with X-ray magnetic circular dichroism and reconstructing fluctuating magnetic states through iterative phase-retrieval algorithms (Box 1 Fig. 1a)[58,59]. Incorporating hierarchical clustering analysis enabled HCDI to capture magnetic fluctuations in degenerate stripe domain states with 18 nm spatial resolution and 387 ms temporal resolution[58]. To improve temporal resolution, HCDI was integrated with the pump–probe technique, allowing observation of the nanoscale dynamics of magnetic spin textures in cobalt–palladium multilayers on femtosecond timescales[59]. Furthermore, X-ray ptychography was combined with pump–probe laminography to capture the 3D magnetization dynamics in a GdCo thin film[27], achieving a lateral resolution of 50 nm and a temporal resolution of 70 ps. These experiments highlight the great potential of CDI and ptychography for quantitatively imaging the 3D structure and dynamics of spin textures with high spatiotemporal resolution.

Beyond imaging magnetic spin textures, single-shot CDI has also been used to visualize quantum vortices in superfluid helium droplets using intense femtosecond XFEL pulses[60]. Helium-4 droplets with radii ranging from 100 nm to 1 μm were generated and injected into an XFEL beam. As they passed through the vacuum, evaporative cooling reduced the droplet temperature below the superfluid transition temperature. Some individual droplets were intercepted by the XFEL pulses, producing single-shot coherent X-ray diffraction patterns. A representative diffraction pattern of a helium-4 droplet doped with xenon atoms to enhance the diffraction contrast is shown in Fig. 3d. The distribution of the Bragg spots indicates that the xenon atoms condensed around the cores of multiple quantum vortices, forming an equilateral triangular lattice within the superfluid droplet (Fig. 3d, inset). Following this experiment, a series of studies were conducted[147,148], including the use of iterative phase retrieval (Box 1) to reconstruct the droplet shapes and the spatial arrangement of xenon-doped quantum vortices[149]. Another quantum material investigated using CDI is VO_2, which undergoes a prototypical insulator–metal transition when heated or excited by an ultrafast laser pulse[61,150]. Pump–probe HCDI, coupled with resonant X-ray spectroscopy, captured the light-induced phase transition in VO_2 with a spatial resolution of 50 nm and a temporal resolution of 150 fs (ref. 61). This approach revealed a distinct structural evolution model, shedding light on the insulator–metal transition in VO_2. These experimental results demonstrate that CDI and ptychography are powerful tools for imaging quantum materials across various length- and timescales.

3D nanoscale imaging of electrodes, nanomaterials and integrated circuits

Lithium-rich layered oxides stand out as one of the most promising cathode materials for the next generation of lithium-ion batteries because of their high energy density and cost-effectiveness. However, their commercialization has been hindered by rapid voltage decay during cycling[31]. Overcoming this obstacle requires a fundamental understanding of the underlying mechanism of voltage decay. In situ BCDI has been used to image the 3D structural dynamics of lithium- and manganese-rich (LMR) layered oxides at the nanoscale, revealing the origin of their structural degradation during cycling[31]. Figure 3e–h shows the 3D lattice displacement and strain evolution of an LMR primary particle during the electrochemical reaction, captured by in situ BCDI. The LMR primary particle comprises two coherent domains: $LiTMO_2$ (where TM stands for the transition metals nickel, manganese and cobalt) and $LiMnO_3$. The pristine structure of the particle displays both compressive and tensile strain. After the initiation of delithiation, tensile strain begins to accumulate on the surface of the $LiTMO_2$ domains (Fig. 3f), where lithium extraction initially takes place. With continuous lithium extraction, the tensile strain increases and extends into the interior of the $LiTMO_2$ domains. When almost all the $LiTMO_2$ domains are delithiated, the tensile strain reaches its maximum and spreads through almost the entire particle (Fig. 3g). With further increase in voltage, the $LiMnO_3$ domains are activated, triggering oxygen release and transition-metal migration, thereby reducing the tensile strain (Fig. 3h). This experiment elegantly demonstrates that severe lattice strain accumulation in LMR cathodes during cycling drives structural degradation and oxygen loss. These findings have been reinforced by further experimental measurements and DFT calculations[31]. As in situ and operando BCDI emerge as a primary tool to probe the 3D lattice displacement and strain evolution in electrodes at the nanoscale[29,31], X-ray ptychography has been integrated with spectroscopy and tomography to visualize 3D structure, morphology and chemical states with high spatial and energy resolution[30,32,151]. Together, these methods are uniquely positioned to tackle some fundamental problems in heterogeneous electrode materials.

CDI and ptychography have also been used to image the structure and dynamics of various nanomaterials[36,62,63,69,70,87,88,152,153]. For instance, in situ BCDI has been employed to capture 3D grain dynamics during heating and 3D dislocation evolution during crystal growth and dissolution[36,153]. X-ray ptychography has been combined with tomography to determine the 3D structure of nanoparticle superlattices and multi-element frameworks engineered by DNA origami, achieving a half-pitch resolution of 7 nm (ref. 62) (Fig. 3i). This resolution enabled the identification of the 3D coordinates of individual nanoparticles and the quantitative characterization of point defects, dislocations, surface reconstruction and grain boundaries in the superlattice. By using extremely short and intense XFEL pulses, single-shot CDI has been used to capture the shapes, facets and morphology of nanoparticles at femtosecond timescales[63,154]. The technique has also been combined with the pump–probe technique to image ultrafast phenomena, such as lattice dynamics and irreversible melting in individual nanocrystals[69,70,155]. By leveraging advanced synchrotron radiation, XFELs and HHG, CDI and ptychography have emerged as powerful methods for studying the structure and dynamics of nanomaterials with high spatiotemporal resolution.

Beyond material characterization, X-ray ptychography has become an important metrology tool for the 3D visualization of modern nanoelectronics, such as integrated circuits[64–66]. Defect inspection, failure analysis and reverse engineering of integrated circuits necessitate 3D imaging metrology across various length scales. The conventional method relies on a combination of optical microscopy, electron microscopy and ion milling techniques, often involving destructive sample preparation. X-ray CDI and ptychography can achieve higher resolution than optical microscopy and image thicker samples than electron microscopy, making them well suited for the non-destructive examination of integrated circuits. After the initial experiment of imaging an IBM integrated circuit with Fresnel CDI[156], there was a breakthrough in 2017. Ptychographic X-ray tomography was used for the non-destructive 3D imaging of an Intel Pentium processor, achieving a half-pitch resolution of 14.6 nm with a diameter of 10 μm (ref. 64). Furthermore, by leveraging the planar geometry of integrated circuits, X-ray ptychography was combined with laminography to visualize not only the 3D volume of an entire chip, but also to provide high-resolution 3D images of magnified subregions[65].

Improvements in ptychographic X-ray tomography since then have enabled the quantitative 3D imaging of a 7 nm commercial integrated circuit[66]. By fabricating the circuit into a cylinder with a diameter of

5 µm, a half-pitch resolution of 4.2 nm (a Rayleigh resolution of 8.4 nm) was achieved. This was made possible by two key innovations: burst ptychography, which captures multiple low-exposure diffraction frames at each scanning position, and digital refocusing of projections to extend the depth of field[66]. These developments greatly increased the imaging volume, resolution and data acquisition speed. The quantitative 3D reconstruction of the lowest layer, detailing the gates, contacts and fins, is shown in Fig. 3j. A cross-section and line scan display the electron-density variation of the 30 nm fin pitch (Fig. 3k,l). This breakthrough highlights the potential of ptychographic X-ray tomography for the non-destructive imaging of complex microelectronic devices and paves the way for future increases in resolution.

Quantitative phase imaging of biological specimens

Biological objects vary greatly in size, spanning seven orders of magnitude from bones and tissues to cells, cellular organelles, viruses and proteins. Visualizing their structures therefore normally requires different imaging modalities. However, CDI and modern ptychography methods offer a solution to this multi-length scale problem by unifying different imaging techniques with the same principle and similar phase-retrieval algorithms (Box 1). Figure 4a,b showcases quantitative phase imaging of a tissue with a 120 mm^2 FOV and 370 nm resolution, obtained using FP[67]. By digital refocusing in post-data analysis, this method can achieve both a large FOV and high resolution for imaging thick biological samples[19]. When combined with ankylography[120], multislice reconstruction[123] and diffraction tomography[138], FP becomes a non-invasive and label-free 3D imaging tool for biomedical applications[41,139,140]. Figure 4c,d illustrates the quantitative 3D reconstruction of the refractive index of unstained HeLa cells, revealing the nuclei, cytoskeletal fibres and cytoplasmic organelles within the cells. The method achieved lateral and depth resolutions of 390 nm and 899 nm, respectively, surpassing the capabilities of conventional quantitative phase-imaging techniques[41]. A key advantage of the method is its ability to capture a 3D volume of approximately 1.7×10^{10} voxels, containing 2×10^{14} cells, with a FOV of 1.77 mm^2, without requiring sample tilting or through-focus series. By incorporating rapid data-acquisition schemes such as multiplexed illumination[39,137], this method can be used for in vitro 3D imaging of multicellular organisms and subcellular structures with a large FOV and high resolution.

Compared with FP, X-ray CDI and ptychography offer higher resolution for quantitative imaging of biological samples, including biominerals[35–37], tissues[34,68] and cellular ultrastructure[42–46]. The 3D phase reconstruction of a bone sample obtained by ptychographic X-ray tomography is shown in Fig. 4e, revealing high-contrast osteocyte lacunae (cavities in the bone matrix) and canaliculi (the complex network of channels)[35]. The resolution of the methods is ultimately limited by radiation damage. One approach to mitigate this limitation is to rapidly freeze biological samples at liquid-nitrogen temperature[157–159]. The ptychographic X-ray tomography of frozen–hydrated mouse brain tissue is shown in Fig. 4f,g, revealing myelinated axons, cell nuclei, lysosomal lipofuscin and neuronal pigmented autophagic vacuoles[68]. Ptychographic tomography has also been combined with X-ray fluorescence to image a frozen–hydrated green alga with a lateral resolution of 45 nm and a depth resolution of 55 nm (ref. 46) (Fig. 4h). The 3D fluorescence signals, displaying the distribution of the elements phosphorus, calcium, sulfur, chlorine and potassium inside the cell, were correlated with high-resolution 3D mass density to visualize the cellular ultrastructure without the need for chemical labelling.

For thinner biological samples, considerably higher resolution can be achieved by cryo-electron ptychography[160]. Figure 4i shows the 3D reconstruction of the rotavirus structure from approximately 500 particles at 1.86 nm resolution[51]. The resolution of cryo-electron ptychography has since improved to 5.8 Å by averaging 11,552 apoferritin particles[53]. Compared with cryo-electron microscopy and tomography[157], cryo-electron ptychography offers three advantages. First, it reconstructs the electron probe along with the magnitude and phase of a biological specimen, enhancing image contrast for weakly scattered features and eliminating the need for contrast transfer function correction. Second, the method simultaneously achieves high resolution and a large FOV. Finally, multislice ptychography can be used to image thicker biological samples than cryo-electron tomography can achieve. With further development, the resolution of cryo-electron ptychography will continue to improve, making it a versatile technique for the high-resolution 3D imaging of proteins, viruses and cellular ultrastructure (Table 1).

Another approach to reducing radiation damage is to capture the diffraction pattern of a biological sample using an intense and ultrafast X-ray pulse before the sample is destroyed[78,86]. This diffraction-before-destruction approach, inspired by the development of XFELs[11,15] and the initial CDI experiment[4], spurred the development of two research directions. The first is serial femtosecond crystallography[161], in which a single XFEL pulse generates resolvable Bragg diffraction from a nanocrystal. By collecting diffraction patterns from numerous nanocrystals at various orientations, a 3D diffraction pattern can be assembled and phased to reveal the 3D atomic structure of the nanocrystals. Serial femtosecond crystallography has enabled the determination of protein and small-molecule structures at room temperature[162] and has inspired the development of microcrystal electron diffraction[163]. The second direction is single-particle imaging, in which CDI is combined with XFELs to perform diffractive imaging of cells[164,165], cellular organelles[166] and viruses[48–50]. The 3D reconstruction of the mimivirus, obtained by averaging 198 particles[49], is shown in Fig. 4j. Although the principle of the single-particle imaging method has been computationally and experimentally established, its resolution has thus far been limited to the nanometre scale[50]. This limitation arises because X-rays have scattering cross-sections four to five orders of magnitude lower than those of electrons[2]. Consequently, cryo-electron ptychography offers advantages over X-ray-based CDI methods for imaging thin biological samples at high resolution. Meanwhile, coherent X-ray sources with high brightness are rapidly being developed worldwide[11,15]. By measuring the continuous X-ray diffraction patterns from imperfect microcrystals of the membrane protein complex photosystem II, researchers have improved the resolution of the photosystem II dimer structure from 4.5 Å to 3.5 Å (ref. 52) (Fig. 4k,l). With further development, X-ray CDI methods could become important tools for the high-resolution imaging of biological specimens that are too thick for cryo-electron ptychography.

Future directions

By integrating microscopy with crystallography, CDI and ptychography have revolutionized our understanding of microscopy, leading to widespread scientific applications. Looking ahead, I outline future directions for this multidisciplinary field that are expected to have a greater impact and become accessible to a broader user community. Currently, CDI and ptychography rely predominantly on iterative algorithms to retrieve phase information from diffraction patterns (Box 1). However, practitioners often require algorithmic training and must optimize the parameters to achieve satisfactory results, which limits the accessibility of these powerful methods. Even for experienced users, phase retrieval and image reconstruction can require hours to days, depending on the size and complexity of the data. To address this limitation, we can draw from the crystallography and cryo-electron microscopy communities, which have successfully implemented dedicated software suites using standard file formats, data objects, automation pipelines and graphical interfaces[157,167]. By adopting similar specialized software suites that are currently under development[168,169], we can streamline automated phase retrieval and image reconstruction for CDI and ptychography. Another important and rapidly advancing direction is deep-learning phase retrieval[74,170,171].

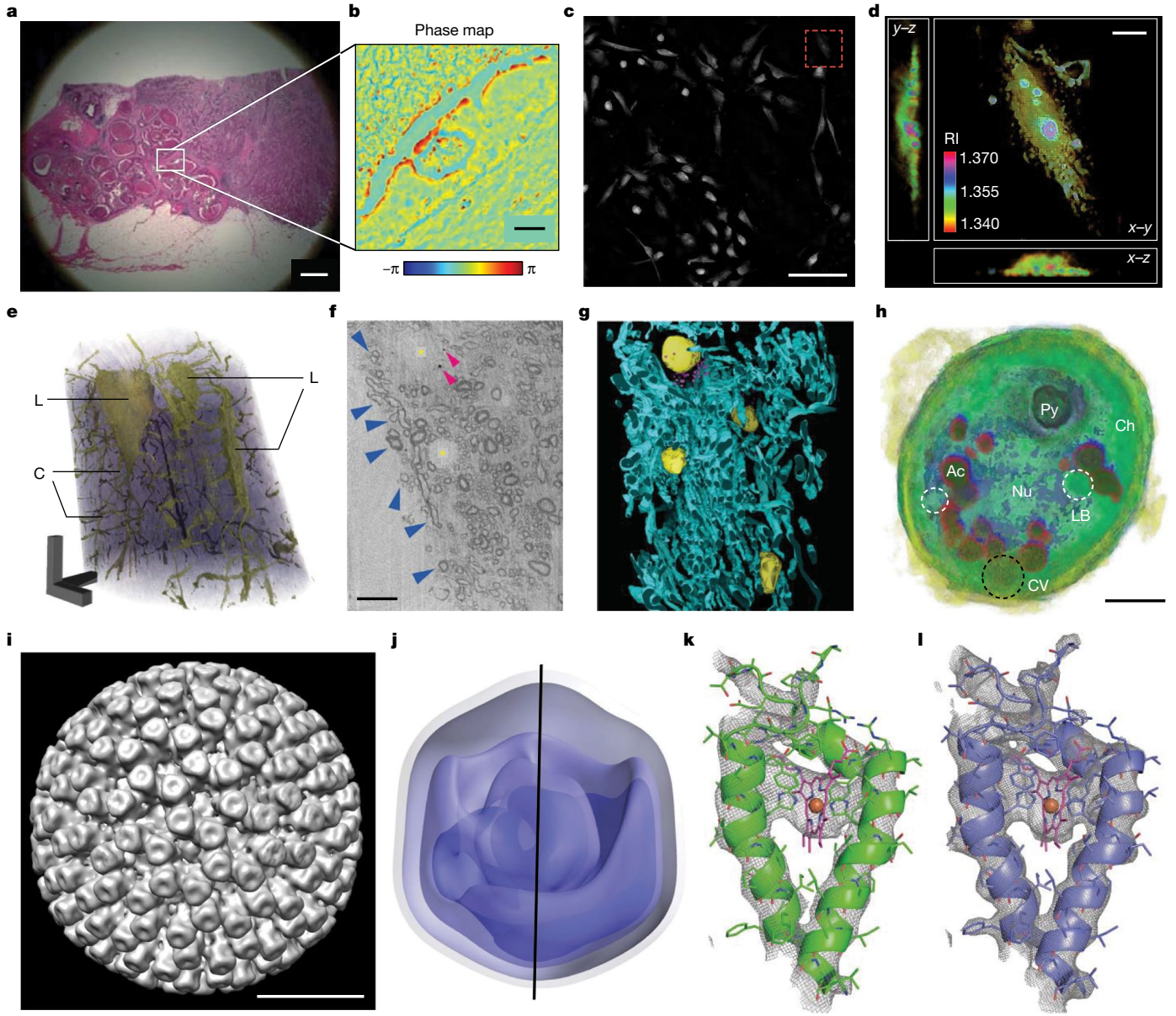

Fig. 4 | Quantitative phase imaging of biological specimens. a, FP image of a tissue with a FOV of 120 mm^2. Scale bar, 1 mm. **b**, Reconstructed phase of the 0.2 mm^2 central region in **a** with a resolution of 370 nm (ref. 67). Scale bar, 40 µm. **c**, 3D reconstruction of the refractive index (RI) of unstained HeLa cells[41], depicted for a selected region within a 1.77 mm^2 FOV at $z = 2.93$ µm. Scale bar, 100 µm. **d**, Magnified 3D view of a cell corresponding to the red square in **c**, with a lateral resolution of 390 nm and a depth resolution of 899 nm. Scale bar, 10 µm. **e**, 3D phase reconstruction of a bone sample with osteocyte lacunae (L) and canaliculi (C) resolved[35]. Scale bars, 5 µm. **f**, 3D imaging of frozen hydrated mouse brain tissue showing myelinated axons (blue arrowheads), cell nuclei (yellow asterisks) and spherical structures (pink arrows)[68]. Scale bar, 10 µm. **g**, 3D segmentation of the reconstructed volume in **f** at the same scale, displaying myelinated axons (blue), cell nuclei (yellow) and spherical structures (pink). **h**, Correlative 3D X-ray fluorescence and ptychographic tomography of a frozen hydrated green alga[46], showing phosphorus-rich regions (dark green), calcium-rich regions (red) and sulfur-rich regions (yellow), with the nucleus (Nu), acidocalcisomes (Ac), pyrenoid (Py), chloroplast (Ch), contractile vacuoles (CVs) and lipid bodies (LB). Scale bar, 2 µm. **i**, 3D reconstruction of the structure of a rotavirus at 1.86 nm resolution using cryo-electron ptychography[51]. Scale bar, 25 nm. **j**, 3D reconstruction of a mimivirus using XFEL-based single-particle imaging[49]. **k**,**l**, Improving the resolution of the photosystem II dimer structure from 4.5 Å (**k**) to 3.5 Å (**l**) by phasing the continuous X-ray diffraction patterns[52]. Images in **a** and **b** reproduced from ref. 67, Elsevier; images in **c** and **d** adapted from ref. 41 under a Creative Commons licence CC BY 4.0; image in **e** reproduced from ref. 35, Springer Nature Limited; images in **f**, **g** and **i** reproduced from refs. 68 (**f** and **g**) and 51 (**i**) under a Creative Commons licence CC BY 4.0; image in **h** reproduced from ref. 46, American Association for the Advancement of Science; image in **j** reproduced from ref. 49. American Physical Society; and images in **k** and **l** reproduced from ref. 52, Springer Nature Limited.

By leveraging powerful neural-network models such as convolutional neural networks, autoencoders and generative adversarial networks, as well as effective learning strategies, these methods can learn the complex relationship between diffraction patterns and object transmission functions[56,172], bypassing conventional iterative algorithms and offering flexibility in handling large-scale datasets. Deep-learning methods hold the potential to transform phase retrieval in CDI and ptychography, enabling faster and more robust reconstruction of complex structures from diffraction patterns[173–177].

By harnessing advanced phase-retrieval algorithms and state-of-the-art detectors, electron ptychography has achieved record-breaking 2D resolution in recent years[21–23], surpassing aberration-corrected electron microscopy, even when conducted using an uncorrected electron microscope[24]. Implementing automated data-acquisition

and real-time phase retrieval is crucial to broadening the user base for electron ptychography. These advancements will enable routine imaging at sub-ångström resolution, making the technique more accessible and driving its wider adoption across scientific disciplines. An exciting frontier is the determination of the 3D atomic structure of technologically critical materials, especially those comprising dose sensitivity and light atoms such as lithium, carbon, nitrogen and oxygen. Numerical simulations and preliminary experiments demonstrate that pAET is a dose-efficient method with the potential to achieve this goal[107,108,178]. With improvements in sample preparation, automated data acquisition, phase retrieval and tomographic reconstruction, pAET is poised to become a crucial technique for resolving the 3D structure of quantum, energy, polymeric and amorphous materials at atomic resolution. Another important advance is cryo-electron ptychography, which recently achieved a resolution of 5.8 Å (ref. 53). With the optimization of data-acquisition procedures and the advancement of specialized phase-retrieval and 3D image reconstruction algorithms, substantial improvements in resolution are anticipated. Moreover, integrating multislice reconstruction with cryo-electron ptychography holds the potential to capture the 3D ultrastructure of cells and tissues beyond the thickness limits of conventional cryo-electron tomography[157].

With the widespread development of fourth-generation synchrotron radiation, XFELs and HHG sources[11,15,179], an increasing number of dedicated coherent X-ray imaging beamlines and stations are being constructed worldwide. This trend solidifies CDI and ptychography as the primary methods for the quantitative imaging of thick samples with high spatial and temporal resolution. The great increase in X-ray brightness allows BCDI to routinely map the 3D lattice displacement and strain fields of various materials at the nanoscale[29,31,36,69,180]. Meanwhile, ptychographic X-ray tomography enables the visualization of the 3D structure of thick samples, such as electrodes[30,32,151], nanomaterials[62], magnetic materials[26–28], integrated circuits[64–66], bone[35] and neuronal tissue[34,68], with a large FOV and nanoscale resolution. However, the resolution is ultimately limited by radiation damage. Numerical simulations and preliminary experiments have demonstrated that in situ CDI, leveraging coherent interference between a strong beam for illuminating static structures and a weak beam for dynamic structures, could reduce the radiation dose by up to two orders of magnitude compared with conventional CDI and ptychography[181,182]. Thus, developing methods to fully harness the coherence of these bright X-ray sources for low-dose CDI is an important direction for future research. For radiation-hard materials, fourth-generation synchrotron radiation could provide the coherent X-ray flux needed for atomic-resolution CDI. With the ability of X-rays to penetrate samples thicker than electrons and offer elemental, chemical and magnetic contrast, achieving atomic-resolution CDI would be an important breakthrough in X-ray diffraction and imaging, complementing electron ptychography. Moreover, by harnessing ultrafast pulses from XFELs[11,15] and HHGs[179], CDI and ptychography could further increase the spatiotemporal resolution in ultrafast imaging. This improvement is expected to deepen our understanding of dynamic processes such as phase transitions, nucleation, melting, heat and spin transport, crack and shock formation, and lattice and grain dynamics[183].

FP has been established as a powerful tool for the quantitative phase imaging of tissues and cell cultures, offering a larger FOV and higher resolution than conventional optical microscopy[19]. An important future direction is to make this method more accessible to the wider user community by implementing automation pipelines for data acquisition, phase retrieval and image reconstruction. The dedicated software suites developed for X-ray and electron CDI and ptychography can be applied to this sub-field, and vice versa[184]. Furthermore, FP has been integrated with darkfield measurements to enable high-resolution, wide-field imaging using an aberration-corrected analytic phase-retrieval framework[185]. These advancements could establish FP as a standard tool for quantitative phase imaging and disease diagnosis[19]. Another promising direction involves addressing outstanding problems in biology and biomedicine. This includes enhancing 3D resolution for live cell imaging and correlating FP with super-resolution and fluorescence microscopy[19].

While lens-based microscopy has served as a foundational tool in modern science for over three centuries, computational microscopy, encompassing CDI and modern ptychography, has emerged as a transformative force over the past 25 years. These advanced techniques have revolutionized imaging capabilities, breaking resolution records in microscopy, simultaneously achieving high resolution and large fields of view and enabling quantitative imaging of magnetic, quantum and energy materials, catalysts, integrated circuits, and biological specimens. Building on their technical advancements, CDI and ptychography have opened new avenues for addressing critical challenges across a wide range of disciplines, including physics, chemistry, materials science, engineering, nanoscience, and biology. Looking to the future, these methods are set to remain at the forefront of innovation, driving the development of next-generation imaging tools, enabling transformative scientific applications and shaping multidisciplinary research for decades to come.

1. Shapin, S. *The Scientific Revolution* 2nd edn (Univ. Chicago Press, 2018).
2. Hawkes, P. W. & Spence, J. C. H. (eds) *Springer Handbook of Microscopy* (Springer, 2019).
3. Crystallography at 100. *Science* **343** (Special issue), 1091–1116 (2014).
4. Miao, J., Charalambous, P., Kirz, J. & Sayre, D. Extending the methodology of X-ray crystallography to allow imaging of micrometre-sized non-crystalline specimens. *Nature* **400**, 342–344 (1999).
This paper reports on the experimental demonstration of unifying crystallography and microscopy by replacing the physical lens with coherent diffraction and computational algorithms.
5. Sayre, D. in *Imaging Processes and Coherence in Physics* Vol. 112 (eds Schlenker, M. et al.) 229–235 (Springer, 1980).
6. Millane, R. P. Phase retrieval in crystallography and optics. *J. Opt. Soc. Am. A* **7**, 394–411 (1990).
7. Gerchberg, R. W. & Saxton, W. O. A practical algorithm for the determination of phase from image and diffraction plane pictures. *Optik* **35**, 237–246 (1972).
8. Fienup, J. R. Phase retrieval algorithms: a comparison. *Appl. Opt.* **21**, 2758–2769 (1982).
This was the development of error-reduction and input–output algorithms for iterative phase retrieval.
9. Bates, R. H. T. Fourier phase problems are uniquely solvable in more than one dimension. I: Underlying theory. *Optik* **61**, 247–262 (1982).
10. Miao, J., Sayre, D. & Chapman, H. N. Phase retrieval from the magnitude of the Fourier transforms of nonperiodic objects. *J. Opt. Soc. Am. A* **15**, 1662–1669 (1998).
The oversampling ratio was introduced; phase retrieval requires more independently measured points than unknown variables.
11. Willmott, P. *An Introduction to Synchrotron Radiation: Techniques and Applications* 2nd edn (Wiley, 2019).
12. Boyle, W. S. & Smith, G. E. Charge coupled semiconductor devices. *Bell Syst. Tech. J.* **49**, 587–593 (1970).
13. Robinson, I. K. & Harder, R. Coherent X-ray diffraction imaging of strain at the nanoscale. *Nat. Mater.* **8**, 291–298 (2009).
14. Chapman, H. N. & Nugent, K. A. Coherent lensless X-ray imaging. *Nat. Photon.* **4**, 833–839 (2010).
15. Miao, J., Ishikawa, T., Robinson, I. K. & Murnane, M. M. Beyond crystallography: diffractive imaging using coherent x-ray light sources. *Science* **348**, 530–535 (2015).
16. Shechtman, Y. et al. Phase retrieval with application to optical imaging: a contemporary overview. *IEEE Signal Process. Mag.* **32**, 87–109 (2015).
17. Pfeiffer, F. X-ray ptychography. *Nat. Photon.* **12**, 9–17 (2018).
18. Rodenburg, J. & Maiden, A. in *Springer Handbook of Microscopy* (eds Hawkes, P. W. & Spence, J. C. H.) 819–904 (Springer, 2019).
19. Zheng, G., Shen, C., Jiang, S., Song, P. & Yang, C. Concept, implementations and applications of Fourier ptychography. *Nat. Rev. Phys.* **3**, 207–223 (2021).
20. Spence, J. C. H., Howells, M., Marks, L. D. & Miao, J. Lensless imaging: a workshop on "new approaches to the phase problem for non-periodic objects". *Ultramicroscopy* **90**, 1–6 (2001).
21. Jiang, Y. et al. Electron ptychography of 2D materials to deep sub-ångström resolution. *Nature* **559**, 343–349 (2018).
Electron ptychography with EMPAD at 0.39 Å resolution is better than aberration-corrected electron microscopy under the same imaging conditions.
22. Chen, Z. et al. Electron ptychography achieves atomic-resolution limits set by lattice vibrations. *Science* **372**, 826–831 (2021).
23. Yang, W., Sha, H., Cui, J., Mao, L. & Yu, R. Local-orbital ptychography for ultrahigh-resolution imaging. *Nat. Nanotechnol.* **19**, 612–617 (2024).
24. Nguyen, K. X. et al. Achieving sub-0.5-angstrom–resolution ptychography in an uncorrected electron microscope. *Science* **383**, 865–870 (2024).
25. Dong, Z. et al. Visualization of oxygen vacancies and self-doped ligand holes in $La_3Ni_2O_{7-\delta}$. *Nature* **630**, 847–852 (2024).
Multislice ptychography combined with electron energy-loss spectroscopy reveals oxygen vacancies in a high-T_c superconductor ($La_3Ni_2O_{7-\delta}$) and correlates nanoscale stoichiometry with electronic structure.

26. Donnelly, C. et al. Three-dimensional magnetization structures revealed with X-ray vector nanotomography. *Nature* **547**, 328–331 (2017).
This paper reveals the development of X-ray vector ptychographic tomography for the 3D imaging of magnetic configurations around Bloch point singularities.
27. Donnelly, C. et al. Time-resolved imaging of three-dimensional nanoscale magnetization dynamics. *Nat. Nanotechnol.* **15**, 356–360 (2020).
28. Rana, A. et al. Three-dimensional topological magnetic monopoles and their interactions in a ferromagnetic meta-lattice. *Nat. Nanotechnol.* **18**, 227–232 (2023).
29. Singer, A. et al. Nucleation of dislocations and their dynamics in layered oxide cathode materials during battery charging. *Nat. Energy* **3**, 641–647 (2018).
30. Csernica, P. M. et al. Persistent and partially mobile oxygen vacancies in Li-rich layered oxides. *Nat. Energy* **6**, 642–652 (2021).
31. Liu, T. et al. Origin of structural degradation in Li-rich layered oxide cathode. *Nature* **606**, 305–312 (2022).
In situ BCDI reveals that severe lattice strain accumulation in Li- and Mn-rich cathodes during cycling drives structural degradation and oxygen loss.
32. Deng, H. D. et al. Correlative image learning of chemo-mechanics in phase-transforming solids. *Nat. Mater.* **21**, 547–554 (2022).
33. Zheng, G., Horstmeyer, R. & Yang, C. Wide-field, high-resolution Fourier ptychographic microscopy. *Nat. Photon.* **7**, 739–745 (2013).
Fourier ptychography was demonstrated by capturing a series of low-resolution intensity images to generate a wide-field, high-resolution complex-valued image.
34. Bosch, C. et al. Non-destructive X-ray tomography of brain tissue ultrastructure. Preprint at *bioRxiv* https://doi.org/10.1101/2023.11.16.567403 (2023).
35. Dierolf, M. et al. Ptychographic X-ray computed tomography at the nanoscale. *Nature* **467**, 436–439 (2010).
36. Clark, J. N. et al. Three-dimensional imaging of dislocation propagation during crystal growth and dissolution. *Nat. Mater.* **14**, 780–784 (2015).
37. Lo, Y. H. et al. X-ray linear dichroic ptychography. *Proc. Natl Acad. Sci. USA* **118**, e2019068118 (2021).
38. Marrison, J., Räty, L., Marriott, P. & O'Toole, P. Ptychography – a label free, high-contrast imaging technique for live cells using quantitative phase information. *Sci Rep.* **3**, 2369 (2013).
39. Tian, L. et al. Computational illumination for high-speed in vitro Fourier ptychographic microscopy. *Optica* **2**, 904–911 (2015).
40. Sun, J., Zuo, C., Zhang, L. & Chen, Q. Resolution-enhanced Fourier ptychographic microscopy based on high-numerical-aperture illuminations. *Sci Rep.* **7**, 1187 (2017).
41. Zuo, C., Sun, J., Li, J., Asundi, A. & Chen, Q. Wide-field high-resolution 3D microscopy with Fourier ptychographic diffraction tomography. *Opt. Lasers Eng.* **128**, 106003 (2020).
42. Miao, J. et al. Imaging whole *Escherichia coli* bacteria by using single particle x-ray diffraction. *Proc. Natl Acad. Sci. USA* **100**, 110–112 (2003).
43. Shapiro, D. et al. Biological imaging by soft x-ray diffraction microscopy. *Proc. Natl Acad. Sci. USA* **102**, 15343–15346 (2005).
44. Giewekemeyer, K. et al. Quantitative biological imaging by ptychographic x-ray diffraction microscopy. *Proc. Natl Acad. Sci. USA* **107**, 529–534 (2010).
45. Jiang, H. et al. Quantitative 3D imaging of whole, unstained cells by using X-ray diffraction microscopy. *Proc. Natl Acad. Sci. USA* **107**, 11234–11239 (2010).
46. Deng, J. et al. Correlative 3D x-ray fluorescence and ptychographic tomography of frozen-hydrated green algae. *Sci. Adv.* **4**, eaau4548 (2018).
47. Song, C. et al. Quantitative imaging of single, unstained viruses with coherent X-rays. *Phys. Rev. Lett.* **101**, 158101 (2008).
48. Seibert, M. M. et al. Single mimivirus particles intercepted and imaged with an X-ray laser. *Nature* **470**, 78–81 (2011).
49. Ekeberg, T. et al. Three-dimensional reconstruction of the giant mimivirus particle with an X-ray free-electron laser. *Phys. Rev. Lett.* **114**, 098102 (2015).
50. Hosseinizadeh, A. et al. Conformational landscape of a virus by single-particle X-ray scattering. *Nat. Methods* **14**, 877–881 (2017).
51. Pei, X. et al. Cryogenic electron ptychographic single particle analysis with wide bandwidth information transfer. *Nat. Commun.* **14**, 3027 (2023).
52. Ayyer, K. et al. Macromolecular diffractive imaging using imperfect crystals. *Nature* **530**, 202–206 (2016).
53. Küçükoğlu, B. et al. Low-dose cryo-electron ptychography of proteins at sub-nanometer resolution. *Nat. Commun.* **15**, 8062 (2024).
54. Jacobsen, C. *X-Ray Microscopy* (Cambridge Univ. Press, 2019).
55. Fannjiang, A. & Strohmer, T. The numerics of phase retrieval. *Acta Numer.* **29**, 125–228 (2020).
56. Dong, J. et al. Phase retrieval: from computational imaging to machine learning: a tutorial. *IEEE Signal Process. Mag.* **40**, 45–57 (2023).
57. Chen, Z. et al. Lorentz electron ptychography for imaging magnetic textures beyond the diffraction limit. *Nat. Nanotechnol.* **17**, 1165–1170 (2022).
58. Klose, C. et al. Coherent correlation imaging for resolving fluctuating states of matter. *Nature* **614**, 256–261 (2023).
59. Zayko, S. et al. Ultrafast high-harmonic nanoscopy of magnetization dynamics. *Nat. Commun.* **12**, 6337 (2021).
60. Gomez, L. F. et al. Shapes and vorticities of superfluid helium nanodroplets. *Science* **345**, 906–909 (2014).
61. Johnson, A. S. et al. Ultrafast X-ray imaging of the light-induced phase transition in VO_2. *Nat. Phys.* **19**, 215–220 (2023).
62. Michelson, A. et al. Three-dimensional visualization of nanoparticle lattices and multimaterial frameworks. *Science* **376**, 203–207 (2022).
63. Xu, R. et al. Single-shot three-dimensional structure determination of nanocrystals with femtosecond X-ray free-electron laser pulses. *Nat. Commun.* **5**, 4061 (2014).
64. Holler, M. et al. High-resolution non-destructive three-dimensional imaging of integrated circuits. *Nature* **543**, 402–406 (2017).
65. Holler, M. et al. Three-dimensional imaging of integrated circuits with macro- to nanoscale zoom. *Nat. Electron.* **2**, 464–470 (2019).
66. Aidukas, T. et al. High-performance 4-nm-resolution X-ray tomography using burst ptychography. *Nature* **632**, 81–88 (2024).
Innovative advancements in ptychographic X-ray tomography enabled the quantitative 3D imaging of a 7-nm commercial integrated circuit, paving the way for future resolution enhancements.
67. Horstmeyer, R., Ou, X., Zheng, G., Willems, P. & Yang, C. Digital pathology with Fourier ptychography. *Comput. Med. Imaging Graph.* **42**, 38–43 (2015).
68. Shahmoradian, S. H. et al. Three-dimensional imaging of biological tissue by cryo X-ray ptychography. *Sci Rep.* **7**, 6291 (2017).
69. Clark, J. N. et al. Ultrafast three-dimensional imaging of lattice dynamics in individual gold nanocrystals. *Science* **341**, 56–59 (2013).
70. Ihm, Y. et al. Direct observation of picosecond melting and disintegration of metallic nanoparticles. *Nat. Commun.* **10**, 2411 (2019).
71. Williams, G. J. et al. Fresnel coherent diffractive imaging. *Phys. Rev. Lett.* **97**, 025506 (2006).
72. Zhang, F. et al. Phase retrieval by coherent modulation imaging. *Nat. Commun.* **7**, 13367 (2016).
73. Latychevskaia, T., Longchamp, J.-N. & Fink, H.-W. When holography meets coherent diffraction imaging. *Opt. Express* **20**, 28871–28892 (2012).
74. Rivenson, Y., Zhang, Y., Günaydın, H., Teng, D. & Ozcan, A. Phase recovery and holographic image reconstruction using deep learning in neural networks. *Light Sci. Appl.* **7**, 17141 (2018).
75. Miao, J. et al. High resolution 3D X-ray diffraction microscopy. *Phys. Rev. Lett.* **89**, 088303 (2002).
76. Marchesini, S. et al. X-ray image reconstruction from a diffraction pattern alone. *Phys. Rev. B* **68**, 140101 (2003).
77. Chapman, H. N. et al. High-resolution ab initio three-dimensional X-ray diffraction microscopy. *J. Opt. Soc. Am. A Opt. Image Sci. Vis.* **23**, 1179–1200 (2006).
78. Chapman, H. N. et al. Femtosecond diffractive imaging with a soft-X-ray free-electron laser. *Nat. Phys.* **2**, 839–843 (2006).
Single-shot coherent X-ray diffractive imaging was demonstrated by capturing an XFEL diffraction pattern before the sample was destroyed.
79. Sandberg, R. L. et al. Lensless diffractive imaging using tabletop coherent high-harmonic soft-X-ray beams. *Phys. Rev. Lett.* **99**, 098103 (2007).
80. Sandberg, R. L. et al. High numerical aperture tabletop soft x-ray diffraction microscopy with 70-nm resolution. *Proc. Natl Acad. Sci. USA* **105**, 24–27 (2008).
81. Ravasio, A. et al. Single-shot diffractive imaging with a table-top femtosecond soft X-ray laser-harmonics source. *Phys. Rev. Lett.* **103**, 028104 (2009).
82. Miao, J., Ohsuna, T., Terasaki, O., Hodgson, K. O. & O'Keefe, M. A. Atomic resolution three-dimensional electron diffraction microscopy. *Phys. Rev. Lett.* **89**, 155502 (2002).
83. Zuo, J. M., Vartanyants, I., Gao, M., Zhang, R. & Nagahara, L. A. Atomic resolution imaging of a carbon nanotube from diffraction intensities. *Science* **300**, 1419–1421 (2003).
84. Huang, W. J., Zuo, J. M., Jiang, B., Kwon, K. W. & Shim, M. Sub-ångström-resolution diffractive imaging of single nanocrystals. *Nat. Phys.* **5**, 129–133 (2009).
85. De Caro, L., Carlino, E., Caputo, G., Cozzoli, P. D. & Giannini, C. Electron diffractive imaging of oxygen atoms in nanocrystals at sub-ångström resolution. *Nat. Nanotechnol.* **5**, 360–365 (2010).
86. Neutze, R., Wouts, R., van der Spoel, D., Weckert, E. & Hajdu, J. Potential for biomolecular imaging with femtosecond X-ray pulses. *Nature* **406**, 752–757 (2000).
87. Robinson, I. K., Vartanyants, I. A., Williams, G. J., Pfeifer, M. A. & Pitney, J. A. Reconstruction of the shapes of gold nanocrystals using coherent x-ray diffraction. *Phys. Rev. Lett.* **87**, 195505 (2001).
88. Pfeifer, M. A., Williams, G. J., Vartanyants, I. A., Harder, R. & Robinson, I. K. Three-dimensional mapping of a deformation field inside a nanocrystal. *Nature* **442**, 63–66 (2006).
Bragg CDI was demonstrated for quantitative 3D imaging of lattice strain at the nanoscale.
89. Marathe, S. et al. Coherent diffraction surface imaging in reflection geometry. *Opt. Express* **18**, 7253–7262 (2010).
90. Roy, S. et al. Lensless X-ray imaging in reflection geometry. *Nat. Photon.* **5**, 243–245 (2011).
91. Sun, T., Jiang, Z., Strzalka, J., Ocola, L. & Wang, J. Three-dimensional coherent X-ray surface scattering imaging near total external reflection. *Nat. Photon.* **6**, 586–590 (2012).
92. Yang, Y. & Sinha, S. K. Three-dimensional imaging using coherent x rays at grazing incidence geometry. *J. Opt. Soc. Am. A Opt. Image Sci. Vis.* **40**, 1500–1506 (2023).
93. Seaberg, M. D. et al. Tabletop nanometer extreme ultraviolet imaging in an extended reflection mode using coherent Fresnel ptychography. *Optica* **1**, 39–44 (2014).
94. Zhang, B. et al. High contrast 3D imaging of surfaces near the wavelength limit using tabletop EUV ptychography. *Ultramicroscopy* **158**, 98–104 (2015).
95. Tanksalvala, M. et al. Nondestructive, high-resolution, chemically specific 3D nanostructure characterization using phase-sensitive EUV imaging reflectometry. *Sci. Adv.* **7**, eabd9667 (2021).
96. Abbey, B. et al. Keyhole coherent diffractive imaging. *Nat. Phys.* **4**, 394–398 (2008).
97. Kfir, O. et al. Nanoscale magnetic imaging using circularly polarized high-harmonic radiation. *Sci. Adv.* **3**, eaao4641 (2017).
98. Broennimann, C. et al. The PILATUS 1M detector. *J. Synchrotron Radiat.* **13**, 120–130 (2006).
99. Tate, M. W. et al. High dynamic range pixel array detector for scanning transmission electron microscopy. *Microsc. Microanal.* **22**, 237–249 (2016).
100. Grimes, M. et al. Bragg coherent diffraction imaging with the CITIUS charge-integrating detector. *J. Appl. Crystallogr.* **56**, 1032–1037 (2023).
101. Miao, J., Förster, F. & Levi, O. Equally sloped tomography with oversampling reconstruction. *Phys. Rev. B* **72**, 052103 (2005).
102. Scott, M. C. et al. Electron tomography at 2.4-ångström resolution. *Nature* **483**, 444–447 (2012).
The experimental demonstration of atomic electron tomography at 2.4 Å resolution was enabled by an advanced computational algorithm.

103. Miao, J., Ercius, P. & Billinge, S. J. L. Atomic electron tomography: 3D structures without crystals. *Science* **353**, aaf2157 (2016).
104. Pham, M., Yuan, Y., Rana, A., Osher, S. & Miao, J. Accurate real space iterative reconstruction (RESIRE) algorithm for tomography. *Sci Rep.* **13**, 5624 (2023).
105. Yang, Y. et al. Determining the three-dimensional atomic structure of an amorphous solid. *Nature* **592**, 60–64 (2021).
The 3D atomic structure of a metallic glass was determined by atomic electron tomography, revealing both short- and medium-range order in the atomic arrangement.
106. Yuan, Y. et al. Three-dimensional atomic packing in amorphous solids with liquid-like structure. *Nat. Mater.* **21**, 95–102 (2022).
107. Chang, D. J. et al. Ptychographic atomic electron tomography: towards three-dimensional imaging of individual light atoms in materials. *Phys. Rev. B* **102**, 174101 (2020).
108. Pelz, P. M. et al. Solving complex nanostructures with ptychographic atomic electron tomography. *Nat. Commun.* **14**, 7906 (2023).
109. Hoppe, W. Diffraction in inhomogeneous primary wave fields: 1. Principle of phase determination from electron diffraction interference [in German]. *Acta Crystallogr. A* **25**, 495–501 (1969).
110. Hoppe, W. Diffraction in inhomogeneous primary wave fields: 3. Amplitude and phase determination for nonperiodic objects [in German]. *Acta Crystallogr. A* **25**, 508–515 (1969).
111. Rodenburg, J. M. & Bates, R. H. T. The theory of super-resolution electron microscopy via Wigner-distribution deconvolution. *Philos. Trans. A Math. Phys. Eng. Sci.* **339**, 521–553 (1992).
112. Nellist, P. D., McCallum, B. C. & Rodenburg, J. M. Resolution beyond the 'information limit' in transmission electron microscopy. *Nature* **374**, 630–632 (1995).
113. Chapman, H. N. Phase-retrieval X-ray microscopy by Wigner-distribution deconvolution. *Ultramicroscopy* **66**, 153–172 (1996).
114. Rodenburg, J. M. et al. Hard-X-ray lensless imaging of extended objects. *Phys. Rev. Lett.* **98**, 034801 (2007).
Modern ptychography was demonstrated by scanning an X-ray probe across an extended sample and using an iterative phase-retrieval algorithm to reconstruct its complex transmission function.
115. Faulkner, H. M. L. & Rodenburg, J. M. Movable aperture lensless transmission microscopy: a novel phase retrieval algorithm. *Phys. Rev. Lett.* **93**, 023903 (2004).
116. Thibault, P. et al. High-resolution scanning X-ray diffraction microscopy. *Science* **321**, 379–382 (2008).
This is the experimental demonstration of reconstructing the complex-valued probe and sample functions using iterative phase retrieval in modern ptychography.
117. Thibault, P. & Menzel, A. Reconstructing state mixtures from diffraction measurements. *Nature* **494**, 68–71 (2013).
118. Guizar-Sicairos, M. & Fienup, J. R. Phase retrieval with transverse translation diversity: a nonlinear optimization approach. *Opt. Express* **16**, 7264–7278 (2008).
119. Maiden, A. M., Humphry, M. J., Sarahan, M. C., Kraus, B. & Rodenburg, J. M. An annealing algorithm to correct positioning errors in ptychography. *Ultramicroscopy* **120**, 64–72 (2012).
120. Raines, K. S. et al. Three-dimensional structure determination from a single view. *Nature* **463**, 214–217 (2010).
121. Wei, H. Fundamental limits of 'ankylography' due to dimensional deficiency. *Nature* **480**, E1 (2011).
122. Wang, G., Yu, H., Cong, W. & Katsevich, A. Non-uniqueness and instability of 'ankylography'. *Nature* **480**, E2–E3 (2011).
123. Maiden, A. M., Humphry, M. J. & Rodenburg, J. M. Ptychographic transmission microscopy in three dimensions using a multi-slice approach. *J. Opt. Soc. Am. A Opt. Image Sci. Vis.* **29**, 1606–1614 (2012).
124. Suzuki, A. et al. High-resolution multislice X-ray ptychography of extended thick objects. *Phys. Rev. Lett.* **112**, 053903 (2014).
125. O'Leary, C. M. et al. Three-dimensional structure of buried heterointerfaces revealed by multislice ptychography. *Phys. Rev. Appl.* **22**, 014016 (2024).
126. Ophus, C. Four-dimensional scanning transmission electron microscopy (4D-STEM): from scanning nanodiffraction to ptychography and beyond. *Microsc. Microanal.* **25**, 563–582 (2019).
127. Lozano, J. G., Martinez, G. T., Jin, L., Nellist, P. D. & Bruce, P. G. Low-dose aberration-free imaging of Li-rich cathode materials at various states of charge using electron ptychography. *Nano Lett.* **18**, 6850–6855 (2018).
128. Song, J. et al. Atomic resolution defocused electron ptychography at low dose with a fast, direct electron detector. *Sci Rep.* **9**, 3919 (2019).
129. O'Leary, C. M. et al. Phase reconstruction using fast binary 4D STEM data. *Appl. Phys. Lett.* **116**, 124101 (2020).
130. Chen, Z. et al. Mixed-state electron ptychography enables sub-angstrom resolution imaging with picometer precision at low dose. *Nat. Commun.* **11**, 2994 (2020).
131. Peng, X. et al. Observation of formation and local structures of metal-organic layers via complementary electron microscopy techniques. *Nat. Commun.* **13**, 5197 (2022).
132. Sha, H. et al. Ptychographic measurements of varying size and shape along zeolite channels. *Sci. Adv.* **9**, eadf1151 (2023).
133. Zhang, H. et al. Three-dimensional inhomogeneity of zeolite structure and composition revealed by electron ptychography. *Science* **380**, 633–638 (2023).
134. Kirkland, A. I., Saxton, W. O., Chau, K.-L., Tsuno, K. & Kawasaki, M. Super-resolution by aperture synthesis: tilt series reconstruction in CTEM. *Ultramicroscopy* **57**, 355–374 (1995).
135. Haigh, S. J., Sawada, H. & Kirkland, A. I. Atomic structure imaging beyond conventional resolution limits in the transmission electron microscope. *Phys. Rev. Lett.* **103**, 126101 (2009).
136. Horstmeyer, R. & Yang, C. A phase space model of Fourier ptychographic microscopy. *Opt. Express* **22**, 338–358 (2014).
137. Tian, L., Li, X., Ramchandran, K. & Waller, L. Multiplexed coded illumination for Fourier ptychography with an LED array microscope. *Biomed. Opt. Express* **5**, 2376–2389 (2014).
138. Horstmeyer, R., Chung, J., Ou, X., Zheng, G. & Yang, C. Diffraction tomography with Fourier ptychography. *Optica* **3**, 827–835 (2016).
139. Tian, L. & Waller, L. 3D intensity and phase imaging from light field measurements in an LED array microscope. *Optica* **2**, 104–111 (2015).
140. Chowdhury, S. et al. High-resolution 3D refractive index microscopy of multiple-scattering samples from intensity images. *Optica* **6**, 1211–1219 (2019).
141. Sha, H., Cui, J. & Yu, R. Deep sub-angstrom resolution imaging by electron ptychography with misorientation correction. *Sci. Adv.* **8**, eabn2275 (2022).
142. Moniri, S. et al. Three-dimensional atomic structure and local chemical order of medium- and high-entropy nanoalloys. *Nature* **624**, 564–569 (2023).
143. Yang, Y. et al. Atomic-scale identification of active sites of oxygen reduction nanocatalysts. *Nat. Catal.* **7**, 796–806 (2024).
144. Basov, D. N., Averitt, R. D. & Hsieh, D. Towards properties on demand in quantum materials. *Nat. Mater.* **16**, 1077–1088 (2017).
145. Nagaosa, N. & Tokura, Y. Topological properties and dynamics of magnetic skyrmions. *Nat. Nanotechnol.* **8**, 899–911 (2013).
146. Yang, Y. et al. Deciphering chemical order/disorder and material properties at the single-atom level. *Nature* **542**, 75–79 (2017).
147. Rupp, D. et al. Coherent diffractive imaging of single helium nanodroplets with a high harmonic generation source. *Nat. Commun.* **8**, 493 (2017).
148. Langbehn, B. et al. Three-dimensional shapes of spinning helium nanodroplets. *Phys. Rev. Lett.* **121**, 255301 (2018).
149. Feinberg, A. J. et al. X-ray diffractive imaging of highly ionized helium nanodroplets. *Phys. Rev. Res.* **4**, L022063 (2022).
150. Johnson, A. S. et al. Quantitative hyperspectral coherent diffractive imaging spectroscopy of a solid-state phase transition in vanadium dioxide. *Sci. Adv.* **7**, eabf1386 (2021).
151. Shapiro, D. A. et al. Chemical composition mapping with nanometre resolution by soft X-ray microscopy. *Nat. Photon.* **8**, 765–769 (2014).
152. Kim, D. et al. Active site localization of methane oxidation on Pt nanocrystals. *Nat. Commun.* **9**, 3422 (2018).
153. Yau, A., Cha, W., Kanan, M. W., Stephenson, G. B. & Ulvestad, A. Bragg coherent diffractive imaging of single-grain defect dynamics in polycrystalline films. *Science* **356**, 739–742 (2017).
154. Loh, N. D. et al. Fractal morphology, imaging and mass spectrometry of single aerosol particles in flight. *Nature* **486**, 513–517 (2012).
155. Barty, A. et al. Ultrafast single-shot diffraction imaging of nanoscale dynamics. *Nat. Photon.* **2**, 415–419 (2008).
156. Abbey, B. et al. Quantitative coherent diffractive imaging of an integrated circuit at a spatial resolution of 20 nm. *Appl. Phys. Lett.* **93**, 214101 (2008).
157. Nogales, E. & Mahamid, J. Bridging structural and cell biology with cryo-electron microscopy. *Nature* **628**, 47–56 (2024).
158. Huang, X. et al. Soft X-ray diffraction microscopy of a frozen hydrated yeast cell. *Phys. Rev. Lett.* **103**, 198101 (2009).
159. Rodriguez, J. A. et al. Three-dimensional coherent X-ray diffractive imaging of whole, frozen-hydrated cells. *IUCrJ.* **2**, 575–583 (2015).
160. Zhou, L. et al. Low-dose phase retrieval of biological specimens using cryo-electron ptychography. *Nat. Commun.* **11**, 2773 (2020).
161. Chapman, H. N. et al. Femtosecond X-ray protein nanocrystallography. *Nature* **470**, 73–77 (2011).
Serial femtosecond crystallography was demonstrated to determine protein nanocrystal structures by capturing snapshot diffraction patterns with XFEL pulses.
162. Barends, T. R. M., Stauch, B., Cherezov, V. & Schlichting, I. Serial femtosecond crystallography. *Nat. Rev. Methods Primers* **2**, 59 (2022).
163. Rodriguez, J. A. et al. Structure of the toxic core of α-synuclein from invisible crystals. *Nature* **525**, 486–490 (2015).
164. Kimura, T. et al. Imaging live cell in micro-liquid enclosure by X-ray laser diffraction. *Nat. Commun.* **5**, 3052 (2014).
165. van der Schot, G. et al. Imaging single cells in a beam of live cyanobacteria with an X-ray laser. *Nat. Commun.* **6**, 5704 (2015).
166. Hantke, M. F. et al. High-throughput imaging of heterogeneous cell organelles with an X-ray laser. *Nat. Photon.* **8**, 943–949 (2014).
167. Sheldrick, G. M. A short history of *SHELX*. *Acta Crystallogr. A* **64**, 112–122 (2008).
168. Wakonig, K. et al. *PtychoShelves*, a versatile high-level framework for high-performance analysis of ptychographic data. *J. Appl. Crystallogr.* **53**, 574–586 (2020).
169. Savitzky, B. H. et al. py4DSTEM: a software package for four-dimensional scanning transmission electron microscopy data analysis. *Microsc. Microanal.* **27**, 712–743 (2021).
170. Sinha, A., Lee, J., Li, S. & Barbastathis, G. Lensless computational imaging through deep learning. *Optica* **4**, 1117–1125 (2017).
171. Kappeler, A., Ghosh, S., Holloway, J., Cossairt, O. & Katsaggelos, A. Ptychnet: CNN based fourier ptychography. In *Proc. IEEE Int. Conf. Image Processing* 1712–1716 (IEEE, 2017).
172. Wang, K. et al. On the use of deep learning for phase recovery. *Light Sci. Appl.* **13**, 4 (2024).
173. Cherukara, M. J., Nashed, Y. S. G. & Harder, R. J. Real-time coherent diffraction inversion using deep generative networks. *Sci Rep.* **8**, 16520 (2018).
174. Wu, L. et al. Three-dimensional coherent X-ray diffraction imaging via deep convolutional neural networks. *NPJ Comput. Mater.* **7**, 175 (2021).
175. Chang, D. J. et al. Deep-learning electron diffractive imaging. *Phys. Rev. Lett.* **130**, 016101 (2023).
176. Schloz, M. et al. Deep reinforcement learning for data-driven adaptive scanning in ptychography. *Sci Rep.* **13**, 8732 (2023).
177. Babu, A. V. et al. Deep learning at the edge enables real-time streaming ptychographic imaging. *Nat. Commun.* **14**, 7059 (2023).
178. Lee, J., Lee, M., Park, Y., Ophus, C. & Yang, Y. Multislice electron tomography using four-dimensional scanning transmission electron microscopy. *Phys. Rev. Appl.* **19**, 054062 (2023).
179. Popmintchev, T. et al. Bright coherent ultrahigh harmonics in the keV X-ray regime from mid-infrared femtosecond lasers. *Science* **336**, 1287–1291 (2012).

180. Li, P. et al. 4th generation synchrotron source boosts crystalline imaging at the nanoscale. *Light Sci. Appl.* **11**, 73 (2022).
181. Lo, Y. H. et al. In situ coherent diffractive imaging. *Nat. Commun.* **9**, 1826 (2018).
182. Lu, X. et al. Computational microscopy beyond perfect lenses. *Phys. Rev. E* **110**, 054407 (2024).
183. Young, L. et al. Roadmap of ultrafast x-ray atomic and molecular physics. *J. Phys. B At. Mol. Opt. Phys.* **51**, 032003 (2018).
184. Wakonig, K. et al. X-ray Fourier ptychography. *Sci. Adv.* **5**, eaav0282 (2019).
185. Cao, R., Shen, C. & Yang, C. High-resolution, large field-of-view label-free imaging via aberration-corrected, closed-form complex field reconstruction. *Nat. Commun.* **15**, 4713 (2024).
186. Schnars, U., Falldorf, C., Watson, J. & Jüptner, W. in *Digital Holography and Wavefront Sensing: Principles, Techniques and Applications* 2nd edn (eds Schnars, U. et al.) 39–68 (Springer, 2015).
187. Taylor, G. The phase problem. *Acta Crystallogr. D Biol. Crystallogr.* **59**, 1881–1890 (2003).
188. Sayre, D. Some implications of a theorem due to Shannon. *Acta Crystallogr.* **5**, 843 (1952).
189. Fienup, J. R. Reconstruction of an object from the modulus of its Fourier transform. *Opt. Lett.* **3**, 27–29 (1978).
190. Bruck, Y. M. & Sodin, L. G. On the ambiguity of the image reconstruction problem. *Opt. Commun.* **30**, 304–308 (1979).
191. Hayes, M. H. The reconstruction of a multidimensional sequence from the phase or magnitude of its Fourier transform. *IEEE Trans. Acoust. Speech Signal Process.* **30**, 140–154 (1982).
192. Candès, E. J., Li, X. & Soltanolkotabi, M. Phase retrieval via Wirtinger flow: theory and algorithms. *IEEE Trans. Inf. Theory* **61**, 1985–2007 (2015).
193. Grohs, P., Koppensteiner, S. & Rathmair, M. Phase retrieval: uniqueness and stability. *SIAM Rev.* **62**, 301–350 (2020).
194. Elser, V. Phase retrieval by iterated projections. *J. Opt. Soc. Am. A* **20**, 40–55 (2003).
195. Luke, D. R. Relaxed averaged alternating reflections for diffraction imaging. *Inverse Probl.* **21**, 37–50 (2005).
196. Rodriguez, J. A., Xu, R., Chen, C.-C., Zou, Y. & Miao, J. Oversampling smoothness: an effective algorithm for phase retrieval of noisy diffraction intensities. *J. Appl. Cryst.* **46**, 312–318 (2013).
197. Maiden, A. M. & Rodenburg, J. M. An improved ptychographical phase retrieval algorithm for diffractive imaging. *Ultramicroscopy* **109**, 1256–1262 (2009).
The extended ptychographic iterative engine was developed to simultaneously reconstruct the complex-valued probe and sample functions.
198. Thibault, P. & Guizar-Sicairos, M. Maximum-likelihood refinement for coherent diffractive imaging. *New J. Phys.* **14**, 063004 (2012).
199. Odstrčil, M., Menzel, A. & Guizar-Sicairos, M. Iterative least-squares solver for generalized maximum-likelihood ptychography. *Opt. Express* **26**, 3108–3123 (2018).
200. Szameit, A. et al. Sparsity-based single-shot subwavelength coherent diffractive imaging. *Nat. Mater.* **11**, 455–459 (2012).
201. Candès, E. J., Strohmer, T. & Voroninski, V. PhaseLift: Exact and stable signal recovery from magnitude measurements via convex programming. *Commun. Pure Appl. Math.* **66**, 1241–1274 (2013).
Phase retrieval was formulated as a convex optimization problem, known as PhaseLift, sparking intense research into numerical algorithms in applied mathematics.
202. Waldspurger, I., d'Aspremont, A. & Mallat, S. Phase recovery, MaxCut and complex semidefinite programming. *Math. Program.* **149**, 47–81 (2015).

Acknowledgements I thank C. M. O'Leary, H. Sha and Z. Zhuang for their comments on the paper, C. M. O'Leary and H. Sha for assistance in preparing Box 1 Fig. 1b, and H. Sha for additional help with Figs. 2–4. I acknowledge support from STROBE: a National Science Foundation Science and Technology Center under award DMR 1548924; the US Department of Energy, Office of Science, Basic Energy Sciences, Division of Materials Sciences and Engineering under award DE-SC0010378; the US Air Force Office Multidisciplinary University Research Initiative (MURI) program under award FA9550-23-1-0281; the US Army Research Office MURI program under award. W911NF-18-1-0431; and the NSF under award DMS-1925919.

Competing interests The author declares no competing interests.

Additional information
Correspondence and requests for materials should be addressed to Jianwei Miao.
Peer review information *Nature* thanks Antoine Islegen-Wojdyla and the other, anonymous, reviewer(s) for their contribution to the peer review of this work.
Reprints and permissions information is available at http://www.nature.com/reprints.
Publisher's note Springer Nature remains neutral with regard to jurisdictional claims in published maps and institutional affiliations.